

Local ITG-like Instability in the Two-fluid and Extended MHD Models in Slab Geometry

D. D. Schnack*, D. C. Barnes†, Ping Zhu, C. C. Hegna and C. R. Sovinec

Center for Plasma Theory and Computation

Department of Engineering Physics

University of Wisconsin - Madison

Madison, WI 53706

April 16, 2012

Abstract

We have verified the NIMROD code by direct comparison with analytic solutions for the case of a plasma with uniform equilibrium density and electron temperature, but with a small gradient of the equilibrium ion temperature, in Cartesian slab geometry. Analytic solutions of the two-fluid and Extended MHD equations in the local approximation and ballooning ordering are developed. The requirement that the corresponding ideal MHD solution remain stable places a constraint on the allowable magnitude of the ion temperature gradient for the local approximation to remain valid. Within this constraint, it is found that the system is unstable if $k_{\perp}\rho_i$ is sufficiently large, but still small enough for the fluid model to be valid. Qualitative agreement with kinetic theory requires that both the ion gyro-viscosity and the ion diamagnetic heat flux be included in the model. NIMROD results are presented for this problem and are compared with the growth rates obtained with the local analytic model. With fixed $\beta = \beta_e + \beta_i = 0.05$ reasonable agreement is found for the variation of the growth rate as a function of inverse equilibrium ion temperature scale length $1/L_{Ti0}$, the electron β fraction $0 < f_e = \beta_e/(\beta_i + \beta_e) < 1$, and $k_{\perp}\rho_i$. There is disagreement between the shape of the global eigenfunction obtained with NIMROD and

*Department of Physics

†TriAlpha Corp.

what might be inferred from the spatial variation of the local analytic growth rate. These differences are unexplained, but we speculate that they may be due to breakdown of the local approximation.

1 Introduction

The ion temperature gradient mode, or ITG, is a parallel sound wave that becomes unstable in the presence of an ion temperature gradient and relative drifts between the ions and the electrons. It was first derived from kinetic theory [1, 2], and also from the moment, or fluid, equations by several authors, [2, 3, 4]. It has been reviewed in the context of a cause of anomalous transport in tokamaks [5], and it has become a textbook problem in kinetic theory [6].

The ITG is most virulent in regions where the equilibrium plasma density is almost spatially uniform and the ion pressure is almost all due to the equilibrium ion temperature gradient. With slab geometry, a uniform magnetic field B_0 in the z -direction, a static electric field, and constant density and electron temperature, this theory leads to an approximate cubic dispersion relation of the form

$$(\omega^2 - \omega_{s*}^2)\omega - \omega_{se}^2\omega_{*Ti} = 0, \quad (1)$$

where $\omega_{s*} = k_z C_{s*}$ is the total parallel hybrid sound frequency (using the ion and electron temperatures and the ion mass), $\omega_{se} = k_z C_{se}$ is the parallel electron sound frequency, and $\omega_{*Ti} = (k_y/eB_0)dT_{i0}/dx$, which has the form of the perpendicular ion drift velocity, but enters the theory in completely different way [3]. When $\omega_{*Ti} \ll (C_s^2/C_*^2)\omega$, the balance between the cubic and linear terms leads to a stable parallel sound wave. When $\omega_{s*}^2 \ll \omega^2 \ll (C_*^2/C_{s*}^2)\omega_{*Ti}^2$, the balance is between the cubic term and the constant term. Then

$$\omega^3 = \frac{k_y k_z^2 T_{e0}}{e B_0 M} \frac{dT_{i0}}{dx}, \quad (2)$$

which has three roots $\omega_n = |A|^{1/3} e^{2\pi i n/3}$, $n = 0, 1, 2$; ω_2 has a negative imaginary part. This is the growth rate γ of the ITG; the real part of ω_2 gives the real frequency of the mode. We write $dT_{i0}/dx \sim \eta_i T_{i0}$, so that $\gamma \sim \eta_i^{1/3}$. The ITG is also called the “ η_i mode”. “The [last] term in [Equation (1)] represents an additional pumping of temperature in the ion waves due to transversal [sic] transport of heat in a nonuniform plasma ... The unstable root corresponds to the possibility of always having the additional pumping ... in phase with the growing temperature for the ion sound waves” [2].

The ITG mode is stable with the context of ideal, resistive, and Hall MHD. Instability requires finite Larmor radius (FLR) effects. In contrast, interchange-like modes (e.g., the g -mode) are ideal MHD modes that are stabilized by two-fluid (i.e., Hall) and FLR effects in slab geometry.

1.1 The Extended MHD Model

In terms of non-dimensional variables, the extended MHD equations are

$$\frac{\partial n}{\partial t} = -\nabla \cdot (n\mathbf{V}) , \quad (3)$$

$$Mn \frac{d\mathbf{V}}{dt} = \mathbf{J} \times \mathbf{B} - \frac{1}{2}\beta \nabla p - \frac{1}{2}\beta_i \delta_i \nabla \cdot \mathbf{\Pi}^{gv} , \quad (4)$$

$$\frac{\partial \mathbf{B}}{\partial t} = -\nabla \times \mathbf{E} , \quad (5)$$

$$\mathbf{E} = -\mathbf{V} \times \mathbf{B} + \frac{1}{n} \delta_i \left(\mathbf{J} \times \mathbf{B} - \frac{1}{2}\beta_e \nabla p_e \right) , \quad (6)$$

$$\frac{dp_i}{dt} = -\Gamma_i p_i \nabla \cdot \mathbf{V} - (\Gamma_i - 1) \frac{1}{2} \beta_i \delta_i \nabla \cdot \mathbf{q}_{gv}^i , \quad (7)$$

and

$$\frac{dp_e}{dt} = -\Gamma_e p_e \nabla \cdot \mathbf{V}_e , \quad (8)$$

where $d/dt \equiv \partial/\partial t + \mathbf{V} \cdot \nabla$ is the advective derivative. Length is measured in terms of a characteristic system size a ,¹ density is measured in terms of a characteristic (or mean) density n_0 , the magnetic field in terms of the characteristic value B_0 , and the species pressure is measured in terms of the characteristic pressure p_{s0} , $s = e, i$. The equation of state for each species is $p_s = nT_s$. The species velocity is measured in units of the Alfvén speed $V_A = B_0/\sqrt{\mu_0 n_0 M}$, and time in units of $t_0 = a/V_A$, so that frequency is measured in units of $\omega_A = 1/t_0 = V_A/a$. The total pressure is $p = p_i + p_e$, $\beta_s \equiv 2\mu_0 p_{s0}/B_0^2$, $\beta = \beta_e + \beta_i$, and $\delta_i \equiv d_i/a = c/(\omega_{pi} a)$. Current density is measured in units of $B_0/(\mu_0 a)$, so that $\mathbf{J} = \nabla \times \mathbf{B}$ and $\delta_i \mathbf{J} = n(\mathbf{V} - \mathbf{V}_e)$.

¹In the usual ITG theory there are two physical length scales: L_{Ti0} , the ion temperature gradient scale length; and L_{n0} , the density gradient scale length. If we choose to measure length in units of L_{n0} , then the non-dimensional equations contain the parameter $\eta_i \equiv L_{n0}/L_{Ti0}$, whose value is determined unambiguously from the two equilibrium scale lengths. In the present case the density is constant, and there is only one macroscopic physical length scale (L_{Ti0}); both L_{n0} and η_i are infinite. Instead we have introduced the second (arbitrary) length scale a in order to retain the formal dependence on the parameter η_i , which is now a/L_{Ti0} . The non-dimensional solution will be an unambiguous function of this η_i . This is satisfactory as long as we stick to the non-dimensional variables. However, the frequency is normalized to the Alfvén frequency $\omega_A = V_A/a$, which depends explicitly on the arbitrary scale length a . One can therefore get *any* value of ω , in sec^{-1} , with the proper choice of a , in meters. This situation is unsatisfactory when trying to compare with the result of computations that are performed with physical (SI) units, as we will do in Section 6. In that case we will choose $a = L_{Ti0}$, so that $\eta_i = 1$; the dependence on the gradient scale length then comes from the non-dimensional variables $\alpha_y = k_y L_{Ti0}$, $\alpha_z = k_z L_{Ti0}$ and $\delta_i = d_i/L_{Ti0}$. Since the normalization of the frequency now depends on L_{Ti0} the physical value in sec^{-1} is determined unambiguously. We will follow this procedure in Section 6.

In general, \mathbf{V} is the center of mass velocity, but in this form $m_e = 0$, so \mathbf{V} is the (non-dimensional) ion velocity. The electron velocity $\mathbf{V}_e = \mathbf{V} - \delta_i \mathbf{J}/n$ is used in Equation (8), including the advective derivative of p_e .

The non-dimensional gyro-viscous stress tensor is

$$\mathbf{\Pi}^{gv} = \frac{\eta_3}{2} \left[\hat{\mathbf{b}} \times \mathbf{W} \cdot (\mathbf{1} + 3\hat{\mathbf{b}}\hat{\mathbf{b}}) + \text{transpose} \right] \equiv \frac{\eta_3}{2} \mathbf{F} \cdot \mathbf{W}(\mathbf{V}), \quad (9)$$

where \mathbf{F} is a tensor operator of rank four (the elastic constant tensor), $\eta_3 = p_i/2B$, $\hat{\mathbf{b}} = \mathbf{B}/B$, and

$$\mathbf{W}_{i,j}(\mathbf{V}) = \frac{\partial V_j}{\partial x_i} + \frac{\partial V_i}{\partial x_j} - \frac{2}{3} \delta_{i,j} \nabla \cdot \mathbf{V}, \quad (10)$$

is the rate of strain tensor. The ion diamagnetic heat flux is

$$\mathbf{q}_{gv}^i = \kappa_{gv}^i \hat{\mathbf{b}} \times \nabla T_i. \quad (11)$$

where $\kappa_{gv}^i = (5/2)(p_i/B)$. In unshered slab geometry, the divergence of Eq. (11) can be written as

$$\nabla \cdot \mathbf{q}_{gv}^i = \frac{5}{2} \frac{1}{B_0} \hat{\mathbf{b}} \cdot (\nabla T_i \times \nabla p_i), \quad (12)$$

$$= \frac{5}{2} \frac{T_i}{nB_0} \hat{\mathbf{b}} \cdot (\nabla p_i \times \nabla n). \quad (13)$$

The parameters Γ_i and Γ_e are the ‘‘adiabatic’’ constants for the ions and electrons. Since the characteristic time scale for the ITG is assumed to be long compared with $1/\Omega$, it is customary to assume that the electrons are isothermal, i.e., $\Gamma_e = 1$. However, direct comparison between the theory and the computations require $\Gamma_e = 5/3$. We always take $\Gamma_i = 5/3$.

Equations (9 - 13) describe to lowest order the collisionless ‘‘transport’’ arising from the small but finite ion Larmor radius²; they represent a non-dissipative transport of momentum and energy due to the spatial variation of the magnetic moments of the gyrating ions[11]. Since this ‘‘transport’’ is not a result of particle collisions³, its effects are completely reversible⁴. Equations (3 - 8) become ideal MHD when $\delta_i = 0$.

²There is another term, the *diamagnetic heat stress* (with the same dependence on the ion diamagnetic heat flux as the ‘‘usual’’ gyro-viscous stress has on the velocity), that also enters the ion stress tensor [11, 20, 21, 22]. However, its non-dimensional coefficient is one order higher in $\rho_i/L_{Ti0} \ll 1$ than the velocity dependent gyro-viscous stress and does not affect the results to lowest order. This corresponds to the ‘‘slow dynamics and weak [pressure] anisotropy’’ regime of Ref. [21], with the assumption that the lowest order distribution function is Maxwellian [22], and the additional ‘‘closure’’ relation $q_{\parallel i} = 0$.

³In Refs.[21, 22] the closures given by Equations (9-11) are called ‘‘collisional’’ because they are derived under the assumption that the lowest order distribution function is locally Maxwellian, which can only be maintained as a result of particle collisions. The closure expressions themselves are independent of particle collisions

⁴Both terms provide dispersive corrections to the characteristic Alfvén and sound waves [10].

Various forms of Equations (3 - 8) are now commonly used in linear and non-linear numerical simulation of tokamak plasmas [8, 9]. An important step in the verification of these computational models is to test their ability to detect accurately instabilities such as the ITG that depend intrinsically on two-fluid and FLR effects.

The specific computational model used in this work [8] solves the “primitive” form [10] of Equations (3 - 8) in specified geometry without further assumptions. Verification of these computational results requires direct comparison with the predictions of a theory that makes the minimum number of assumptions. Nonetheless, the complexity of the mathematics involved in solving the analytic model still dictates a number of simplifying assumptions. In particular, the equilibrium in slab geometry has a unidirectional magnetic field $\mathbf{B}(x) = B_0(x)\hat{\mathbf{e}}_z$ that varies only in the x -direction. Perturbations to the equilibrium are assumed to vary as $f = \hat{f}e^{i(\omega t + k_y y + k_z z)}$, where \hat{f} is independent of x . This “local approximation” reduces the problem to algebra. (However, x -derivatives of equilibrium quantities must be included.) Further, since for fusion applications we are primarily interested in frequencies that are comparable with or less than the Alfvén frequency $\omega_A = V_A/a$ and parallel wavelengths that are much longer than perpendicular wavelengths, we can introduce a small parameter $k_z/k_y \sim \epsilon^2 \ll 1$, and assume $\omega/\omega_A \leq 1$. This “ballooning ordering” further simplifies the algebra, and in many cases we obtain a dispersion relation only to lowest order in ϵ . We also take $T_{e0} = \text{constant}$ and $n_0 = \text{constant}$.

1.2 FLR Cancellations

The collisionless, reversible “transport” embodied in the ion gyro-viscous stress, Equation (9), and the ion diamagnetic heat flux heat flux, Equation (11), represent the lowest order (in $k_\perp \rho_i$) effects of finite ion Larmor radius (FLR) when $\beta_i > 0$. These terms cancel, either whole or in part, the terms describing advection by the ion diamagnetic drift velocity $\mathbf{V}_{*i} \cdot \nabla$. This has a significant effect on the stability properties of the extended MHD model.

The first of these occurs within the ion momentum equation, and can be written, in SI units, as $Mn\mathbf{V}_{*i} \cdot \nabla \mathbf{V} + \nabla \cdot \mathbf{\Pi}_i^{gv} \approx 0$. This is called the *gyro-viscous cancellation*, because it involves the ion gyro-viscous force.⁵ This is motivated by the form of the gyro-viscous stress, Equation (9); in cartesian coordinates, the

⁵As pointed out in Ref. [22], “contrary to widespread lore” the cancellation actually involves the magnetization velocity, $\mathbf{V}_M = -(1/en)\nabla \times (p_\perp \hat{\mathbf{b}}/B)$, and not the diamagnetic drift velocity. These are only equal when the magnetic field is constant.

relevant terms of the x -component of the ion momentum equation are (in SI units)

$$i \left(\omega + \frac{k_y}{n_0 e B_0} \frac{dp_{i0}}{dx} \right) V_x = - \frac{1}{M n_0} \frac{\partial \Pi_{xx}^{gv}}{\partial x} \approx \frac{i k_y V_x}{2 n_0 e B_0} \frac{dp_{i0}}{dx} + \dots \quad (14)$$

The gyro-viscous force therefore cancels at least part ($\sim 1/2$) of the advection from the diamagnetic drift. In analytic work the cancellation is often assumed to be complete, i.e., $M n \mathbf{V}_{*i} \cdot \nabla \mathbf{V}_i + \cdot \mathbf{\Pi}_i^{gv} = 0$. This assumption greatly simplifies both the equations and the ensuing algebra (see Refs. [11, 22] for a more thorough discussion). Clearly the situation is more complicated.⁶

The second cancellation, arising from the ion diamagnetic heat flux, involves the ion energy equation, Equation (7), and the ion continuity equation, Equation (18): $(3/2) \nabla \cdot \mathbf{q}_i^{gv}$ cancels the advection of density by the ion diamagnetic drift $\mathbf{V}_{*i} \cdot \nabla n$. This can be seen as follows.

Decompose the (nonlinear) velocity as $\mathbf{V} = \mathbf{V}_i + \mathbf{V}_{*i}$, where $\mathbf{V}_{*i} = \hat{\mathbf{b}} \times \nabla p_i / (n e B)$ is the diamagnetic drift velocity. The velocity \mathbf{V}_i contains all the dynamical parts of the ion flow plus the $E \times B$ drift. Solve Equation (3) for $\nabla \cdot \mathbf{V}_i$ (using $\nabla \cdot \mathbf{V}_{*i} = 0$), and substitute this expression into Equation (7). The result is

$$\begin{aligned} \frac{\partial p_i}{\partial t} + (\mathbf{V}_i + \mathbf{V}_{*i}) \cdot \nabla p_i &= \frac{5}{3} \frac{p_i}{n} \frac{\partial n}{\partial t} + \frac{5}{3} \frac{p_i}{n} \mathbf{V}_i \cdot \nabla n \\ &\quad + \frac{5}{3} \frac{p_i}{n} \mathbf{V}_{*i} \cdot \nabla n - \frac{2}{3} \nabla \cdot \mathbf{q}_i^{gv}. \end{aligned} \quad (15)$$

We concentrate on the last two terms on the right hand side. From the definition of \mathbf{V}_{*i} and $p_i = n T_i$, we have

$$\begin{aligned} \mathbf{V}_{*i} \cdot \nabla n &= \frac{1}{n e B} \hat{\mathbf{b}} \times \nabla p_i \cdot \nabla n \\ &= \frac{1}{e B} \hat{\mathbf{b}} \cdot (\nabla T_i \times \nabla n). \end{aligned} \quad (16)$$

Then using Equation (12),

$$\begin{aligned} \frac{5}{3} \frac{p_i}{n} \mathbf{V}_{*i} \cdot \nabla n - \frac{2}{3} \nabla \cdot \mathbf{q}_i^{gv} &= \frac{5}{3} \frac{T_i}{e B} \hat{\mathbf{b}} \cdot (\nabla T_i \times \nabla n) \\ &\quad - \left(\frac{2}{3} \right) \left(\frac{5}{2} \right) \frac{T_i}{e B} \hat{\mathbf{b}} \cdot (\nabla T_i \times \nabla n) \\ &= 0. \end{aligned} \quad (17)$$

⁶To quote Ref. [21]: “Even for the simplest form of the gyro-viscosity . . . the clutter originating from the numerous remaining terms . . . far outweighs the benefits of the cancellation. Therefore, even though the gyro-viscous cancellation is implicit in our equations, it is deemed advantageous not to be concerned about it.”

Unlike the gyro-viscous cancellation, this cancellation is complete (i.e., exact) for electrostatic modes in unshered slab geometry where $\nabla \times \hat{\mathbf{b}}_0 = 0$; in the more general case the right hand side is $-(2/3)(p_i/eB)\nabla T_i \cdot \nabla \times \hat{\mathbf{b}}$. To our knowledge, this cancellation has no special name in the literature, although it is widely used. For lack of a better term, we refer to it as the *diamagnetic heat cancellation*.

We shall see that both the gyro-viscous cancellation and the diamagnetic heat flux cancellation must be included in the two-fluid model to obtain results consistent with kinetic theory, where they arise naturally.

2 Analytical Model

The theory of the ITG is well-known [1, 2], and has been extended to include the effects of magnetic shear and toroidal geometry [12, 13]. Computational results for the ITG have used gyro-fluid models [14] and gyro-kinetic models [15]. To the best of our knowledge, ITG-like modes have not been previously calculated with an extended MHD model. In order to verify the computational results, it is desirable to have an appropriate analytic solution of these equations. Ideally, this theory would provide an exact solution of the same equations as solved in the computational algorithm. This is impractical, if for no other reason that the resulting analytic model would be a set of differential equations that would need to be solved numerically. Here we attempt to find an *approximate* analytical solution of the extended MHD equations, or their equivalent set of two-fluid equations, that requires as few assumptions as possible while retaining algebraic tractability. We emphasize that we do not intend to present a new theory of the ITG; rather, we find approximate solutions of the extended MHD equations (i.e., the equivalent two-fluid equations) that are as close as practical to those solved in the computational model, and compare them with the numerical solutions.

For the analysis, we use a two-fluid model in which the ions and electrons have individual velocities, temperatures, and pressures, and obey separate continuity, momentum and energy equations. Assuming quasi-neutrality, so that $n_i = n_e = n$, neglecting the electron mass ($m_e = 0$), and using the same normalization as in Equations (3)-(8), these equations are ion continuity,

$$\frac{\partial n}{\partial t} = -\nabla \cdot (n\mathbf{V}_i) , \quad (18)$$

electron continuity,

$$\frac{\partial n}{\partial t} = -\nabla \cdot (n\mathbf{V}_e) , \quad (19)$$

ion momentum,

$$\delta_i n \frac{d\mathbf{V}_i}{dt} = n (\mathbf{E} + \mathbf{V}_i \times \mathbf{B}) - \frac{1}{2} \beta_i \delta_i (\nabla p_i - \delta_i \nabla \cdot \mathbf{\Pi}_i^{gv}) , \quad (20)$$

and electron momentum,

$$0 = -n(\mathbf{E} + \mathbf{V}_e \times \mathbf{B}) - \frac{1}{2}\beta_e \delta_i \nabla p_e , \quad (21)$$

along with Equations (7) (with $\mathbf{V} = \mathbf{V}_i$) and (8). The electric field is

$$\mathbf{E} = \mathbf{E}_0 - \nabla\phi - \frac{\partial \mathbf{A}}{\partial t} , \quad (22)$$

where \mathbf{E}_0 is a constant externally applied field, \mathbf{A} is the vector potential, $\mathbf{B} = \nabla \times \mathbf{A}$, and ϕ is the scalar potential. (Here, \mathbf{E} is measured in units of $V_A B_0$, ϕ is measured in units of $\phi_0 = \Omega a^2 B_0$ and \mathbf{A} is measured in units of $A_0 = B_0 a = E_0 t_0$.) These must be supplemented by Ampère's law, Equation (5), and Faraday's law

$$\delta_i \mathbf{J} = n(\mathbf{V}_i - \mathbf{V}_e) , \quad (23)$$

$$= \delta_i \nabla \times \mathbf{B} . \quad (24)$$

These equations are equivalent to the extended MHD equations, Equations (3-8). Identifying $\mathbf{V} = \mathbf{V}_i$, Equation (18) becomes Equation (3); subtracting Equations (18) and (19) yields $\nabla \cdot \mathbf{J} = 0$, consistent with Equations (23) and (24). Adding Equations (20) and (21) eliminates \mathbf{E} and, using Equation(23), and dividing out a common factor of δ_i , yields Equation (4), while using Equation (23) in Equation (21) yields the extended Ohm's law, Equation (6). (These manipulations also require the electron pressure to be expressed in the ion frame of reference; we omit the details. Further, the required division by δ_i precludes setting $\delta_i = 0$; ideal MHD is obtained directly from Equations (18) - (24) only in the *limit* $\delta_i \rightarrow 0$.)

The equation for the electromagnetic field is found by introducing $\mathbf{B} = \nabla \times \mathbf{A}$ into Equation (24), using Equation (23), and imposing the gauge condition $\nabla \cdot \mathbf{A} = 0$:

$$\delta_i \nabla^2 \mathbf{A} = -n(\mathbf{V}_i - \mathbf{V}_e) . \quad (25)$$

This couples the ion and electron dynamics.

We will determine the stability of the system by considering the evolution of small perturbations about a steady equilibrium (force balance) state. We work in simple slab geometry (x, y, z) , where equilibrium quantities can vary in x ; y and z are periodic coordinates. (In the computations, there are perfectly conducting walls at $x = \pm a$.) We will denote equilibrium quantities by the subscript $(\dots)_0$. The equilibrium is characterized by $\partial/\partial t = 0$ but $\mathbf{V}_{s0} \neq 0$. The magnetic field is $\mathbf{B}_0 = B_0(x)\hat{\mathbf{e}}_z$. The condition for force balance is

$$\frac{d}{dx} [B_0(x)^2 + \beta_i p_{i0}(x) + \beta_e p_{e0}(x)] = 0 , \quad (26)$$

where $B_0(0) = p_{i0}(0) = p_{e0}(0) = 1$. The remaining equilibrium conditions are given by the ion and electron drift velocities

$$V_{sy0}(x) = -\frac{E_{x0}}{B_0(x)} \pm \frac{1}{2} \frac{\beta_s \delta_i}{B_0(x)} \frac{dp_{s0}(x)}{dx}, \quad (27)$$

where the (+) sign is for ions, the (-) sign is for electrons, $p_{s0}(x) = n_0(x)T_{s0}(x)$, and E_{x0} is a constant applied electric field whose value can be chosen arbitrarily (and for convenience), and determines the frame of reference.

In this work we choose the particular functional dependence $n_0(x) = 1$, $T_{e0}(x) = 1$, and $T_{i0}(x) = e^{\eta_i x}$, where $\eta_i \equiv a/L_{Ti}$, and L_{Ti} is the scale length for variations in the ion temperature. Then

$$B_0(x) = \sqrt{1 - \beta_i [e^{\eta_i x} - 1]}, \quad (28)$$

$$V_{iy0}(x) = -\frac{E_{x0}}{B_0(x)} + \frac{\beta_i \delta_i \eta_i}{2B_0(x)} e^{\eta_i x}, \quad (29)$$

and

$$V_{ey0}(x) = -\frac{E_{x0}}{B_0(x)}. \quad (30)$$

From Equation (29), $E_{x0} \sim O(\delta_i)$, and we will sometimes write $E_{x0} = \mathcal{E}_{x0} \delta_i$. This equilibrium is stable in ideal MHD.

We note that Equation (28) requires that

$$\eta_i < \ln \left(\frac{1 + \beta_i}{\beta_i} \right). \quad (31)$$

The linearized non-dimensional two-fluid equations comprise sixteen equations in the sixteen unknowns n (1), \mathbf{V}_i (3), \mathbf{V}_e (3), ϕ (1), p_i (1), p_e (1), \mathbf{A} (3), and \mathbf{B} (3). These are differential equations, and are mathematically equivalent to the equations solved in the computational model [8]. They can be reduced to an algebraic system of equations by assuming the perturbed quantities vary as $f = \hat{f} e^{i(wt + \alpha_y y + \alpha_z z)}$, where $w = \omega/\omega_A$ is the non-dimensional frequency, $\alpha_y = k_y a$ and $\alpha_z = k_z a$ are non-dimensional wave numbers, \hat{f} is assumed to be independent of x , accounting for the x -dependence of the equilibrium quantities, and evaluating the resulting expressions at $x = 0$.

Most analytical studies of two-fluid instabilities such as the ITG proceed by algebraic manipulation of the individual equations of the model, with appropriate approximations made at crucial points in the calculation. In this work we retreat behind formalism. The individual algebraic equations are a homogeneous algebraic system in the unknowns $(n, V_{xi}, V_{yi}, V_{zi}, V_{xe}, V_{ye}, V_{ze}, p_i, p_e, \phi, A_x, A_y, A_z, B_x, B_y, B_z)$.

Non-trivial solutions require that the determinant of the system vanish. This yields an eighth order algebraic equation $F(w) = 0$ for the non-dimensional frequency w ; there are eight roots. The system is stable if all the roots are real. These calculations are enabled by very useful and powerful mathematical software [16].

The equation $F(w) = 0$ can be solved without further approximation in some simple cases. When $\eta_i = 0$ (a uniform medium), $\beta_i = \beta_e = 0$, and $\alpha_y = 0$, $F(w) = 0$ is a quadratic equation in w^2 . There are no FLR effects. When $\alpha_z = 0$, the roots are $w_{\pm}^2 = \alpha_y^2$, which are compressional Alfvén waves. When $\alpha_y = 0$, the roots are

$$w_{\pm}^2 = \alpha_z^2 \left(1 + \frac{1}{2} \alpha_z^2 \delta_i^2 \pm \alpha_z \delta_i \sqrt{1 + \frac{1}{4} \alpha_z^2 \delta_i^2} \right) . \quad (32)$$

The first term is the shear Alfvén wave, the second term is the whistler wave, and the last terms are two fluid corrections ($\sim \alpha_z \delta_i = k_z d_i$). At finite β , when $\alpha_y = 0$ the roots are the usual parallel sound waves $w_{\pm}^2 = (2/3) \alpha_z^2$, and four more complicated roots that contain two fluid and FLR corrections. When $\alpha_z = 0$, the roots are

$$w_{\pm}^2 = \alpha_y^2 \left(1 + \frac{2}{3} \beta + \frac{1}{64} \alpha_y^2 \beta^2 \delta_i^2 \right) . \quad (33)$$

The first two terms are magneto-acoustic waves, and the last term is an FLR correction ($\sim \alpha_y \delta_i \sqrt{\beta/2} = k_y \rho_i$), where $\rho_i = V_{thi}/\Omega$ is the ion gyro-radius.

For other situations the solvability condition is more complicated. We are interested in solutions corresponding to long parallel wavelength, short perpendicular wavelength, and relatively low frequency, on the order of ω_A or less. We therefore introduce a small parameter $\epsilon \ll 1$, and order $\alpha_y \sim 1/\epsilon^2 \gg 1$, $\alpha_z \sim 1$, and $w \sim 1$. We also order $E_{x0} \sim \epsilon^2$ and $\delta_i \sim \epsilon^2$. All other parameters are $O(1)$ or less. Then the solvability condition contains only even powers of ϵ , and can be written as

$$F(w) = F_0(w) + F_2(w)\epsilon^2 + F_4(w)\epsilon^4 + \dots , \quad (34)$$

so that, to lowest order in ϵ , the solvability condition is $F_0(w) = 0$. This is generally a simpler equation (i.e., lower order in w) than $F(w) = 0$, and possibly easier to solve.

2.1 Electrostatic Modes

2.1.1 The Cubic Dispersion Relation

We first consider the electrostatic case, $\mathbf{E} = -\nabla\phi$. Then $F_0(w) = 0$ is a quartic equation in w , which factors as

$$w = \mathcal{E}_{x0} \delta_i \alpha_y , \quad (35)$$

times a cubic $f_3(w) = 0$ of the form

$$a_3 w^3 + 3a_2 w^2 + 3a_1 w + a_0 = 0 . \quad (36)$$

Equation (35) depends explicitly on the equilibrium electric field (the frame of reference) and vanishes when $\mathcal{E}_{x0} = 0$; it is the zero frequency mode $\omega - k_y V_E = 0$ in the Doppler shifted reference frame.

In Equation (36), the individual coefficients a_i are complicated functions of the non-dimensional parameters, and provide little insight. Unlike Equation (1), this equation contains all powers of w up to three. However, the coefficient of the quadratic term, a_2 , is linear in the electric field E_{x0} , and we take advantage of the arbitrariness of the frame of reference by choosing E_{x0} so that $a_2 = 0$. The specific expression for E_{x0} is complicated, and is not given here. (The stability properties of the system are independent of the choice of reference frame, i.e., of E_{x0} , as will be demonstrated.) Then dividing by the coefficient of the cubic term, the equation is of the form⁷

$$w^3 + 3a'_1 w + a'_0 = 0 , \quad (37)$$

which is now in the same form as Equation (1). The new coefficients a'_i are still complicated, and depend on specific assumptions, such as the presence, absence, or completeness of the FLR cancellations discussed in Section 1.2.

Equations of the form

$$x^3 - 3Ax + B = 0 \quad (38)$$

are called *deficient cubics* because of the absence of the quadratic term. They can be solved by using the substitution $x = \sqrt{A}(z + 1/z)$, which transforms Equation (38) into a quadratic equation for z^3 whose roots are⁸

$$z_l = \left(-\frac{B}{2A^{3/2}} + \sqrt{\frac{B^2}{4A^3} - 1} \right)^{1/3} e^{2\pi i l/3}, \quad l = 0, 1, 2 . \quad (39)$$

When $B^2/4A^3 < 1$, z is on the unit circle, so that $z^* = 1/z$, x is real, and the solutions are stable. When $B^2/4A^3 > 1$, z is not on the unit circle, one root is real and two are complex conjugates. The root $l = 2$ has a negative imaginary part⁹ which indicates instability.

Specific cases are considered below.

⁷The general cubic can always be reduced to this form by means of the substitution $w = (z - a_2)/a_3$, see Ref. [7], Chapter 5.

⁸While the cubic has three solutions, the sixth order equation has six solutions. However, three of them are duplicates[7], and the cubic has only three unique roots.

⁹Recall that we use time dependence of $e^{i\omega t}$.

2.1.2 Complete FLR Cancellations

We now assume, as in most previous analyses, that both the gyro-viscous cancellation and the diamagnetic heat cancellation are complete. In this case, this assumption is exact for the diamagnetic heat flux but only approximate for the gyro-viscosity. The coefficients of Equation (37) remain complicated, but to lowest order in the small parameter δ_i , the dispersion relation reduces to

$$w^3 - \frac{1}{2}\alpha_z^2 \left(\beta_e + \frac{5}{3}\beta_i \right) w - \frac{1}{4}\alpha_y\alpha_z^2\beta_i\beta_e\delta_i\eta_i = 0 , \quad (40)$$

which is the non-dimensional form of the standard result, Equation (1). The ‘‘full’’ cubic contains terms that higher order in $k_\perp\rho_i \equiv \alpha_y\delta_i\sqrt{\beta_i/2}$. Equation (40) has the property that its solutions are stable when either $\beta_e = 0$ or $\beta_i = 0$.

The balance of the first two terms in Equation (40) give parallel sound waves,

$$w^2 = \frac{1}{2} \left(\beta_e + \frac{5}{3}\beta_i \right) \alpha_z^2 , \quad (41)$$

while the balance of the second (linear) and third (constant) terms yields a low frequency drift-like wave,

$$w = -2\beta_i \left(1 + \frac{1}{6}\beta_i \right) \eta_i\delta_i\alpha_y , \quad (42)$$

that propagates in the perpendicular (drift) direction. Instability results when the cubic term is balanced by the constant term.

We have seen that the condition $B^2/4A^3 > 1$ is necessary for instability, where A and B are the coefficients appearing in Equation (38). Applying this to Equation (40), the instability condition is

$$\frac{27}{8} \frac{\alpha_y^2\beta_i^2\beta_e^2\delta_i^2\eta_i^2}{\alpha_z^2 \left(\beta_e + \frac{5}{3}\beta_i \right)^3} > 1 . \quad (43)$$

The system will become unstable when $\eta_i > \eta_i^{crit}$, where

$$\eta_i^{crit} = \left(\frac{2}{3} \right)^{3/2} \frac{\alpha_z \left(\beta_e + \frac{5}{3}\beta_i \right)^{3/2}}{\alpha_y \beta_i\beta_e\delta_i} . \quad (44)$$

The condition for instability can also be written as $k_\perp\rho_i > g(\beta_i, \beta_e)k_zL_{Ti0}$. There is a threshold in $k_\perp\rho_i$ for the onset of instability, and instability is facilitated by long parallel wavelength ($\alpha_z/\alpha_y \ll 1$).

In deriving Equation (40), we chose the constant electric field E_{x0} so that the coefficient of the quadratic term vanished, leading to a deficient cubic. If instead

we do not specify E_{x0} , but leave it arbitrary, then to lowest order in ϵ and δ_i we obtain¹⁰

$$w_E^3 - \frac{1}{2}\alpha_z^2 \left(\beta_e + \frac{5}{3}\beta_i \right) w_E - \frac{1}{4}\alpha_y\alpha_z^2\beta_i\beta_e\delta_i\eta_i = 0, \quad (45)$$

where $w_E = w - \alpha_y\delta_i\mathcal{E}_{x0}$. (Setting $w_E = 0$ is the same as Equation (35).) This is identical to Equation (40), so the stability properties of the system are independent of E_{x0} , as claimed previously¹¹. The electric field produces a Doppler shifted frequency because it is equivalent to a coordinate transformation.

The first two terms in Equation (40) (or Equation (45)) produce a parallel sound wave. The constant term, which is responsible for the instability, has its origin in the term $\mathbf{V}_i \cdot \nabla p_{i0}$ in the ion energy equation. This describes advection of the equilibrium pressure by the perturbed ion flow ($V_{xi} dp_{i0}/dx \sim \eta_i$). It is abetted by the z -component of the electron momentum equation (parallel Ohm's law), which leads to a Boltzmann distribution of electron pressure and electrostatic potential along the magnetic field if $\beta_e > 0$. This couples the electron and ion dynamics. These effects can conspire to be in phase with, and reinforce, the pressure perturbations of the sound wave. If dp_{i0}/dx (i.e., η_i) is large enough, and $\beta_e > 0$, this can lead to instability.

2.1.3 Incomplete Gyro-viscous Cancellation

We now consider the case when the gyro-viscous cancellation in the ion momentum equation is incomplete, but the diamagnetic heat cancellation remains complete. This is the most ‘‘physically realistic’’ case for the unsheared slab geometry under consideration. To lowest order in ϵ and δ_i , the dispersion relation is

$$w^3 - \frac{1}{2}\alpha_z^2 \left(\beta_e + \frac{5}{3}\beta_i \right) w - \frac{1}{4}\alpha_y\alpha_z^2\beta_i \left[\beta_e \left(1 + \frac{1}{6}\beta_i \right) + \frac{5}{18}\beta_i^2 \right] \delta_i\eta_i = 0, \quad (46)$$

This allows the possibility of instability when $\beta_e = 0$. However, in that case the constant term is $O(\beta_i^3) \ll 1$ for $\beta_i < 1$. The critical value of η_i for the onset of instability is

$$\eta_i^{crit} = \left(\frac{2}{3} \right)^{3/2} \frac{\alpha_z}{\alpha_y \beta_i} \frac{\left(\beta_e + \frac{5}{3}\beta_i \right)^{3/2}}{\left[\beta_e \left(1 + \frac{1}{6}\beta_i \right) + \frac{5}{18}\beta_i^2 \right] \delta_i}. \quad (47)$$

This differs from Equation (44) by the factor in brackets in the denominator, which is $\sim \beta_e$ when $\beta_i \ll 1$. While this allows the possibility of instability when $\beta_e = 0$, it requires $\eta_i^{crit} \sim 1/\beta_i^3 \gg 1$. When $\beta_e > 0$, Equation (47) agrees very well with Equation (44).

¹⁰The equation is actually a full cubic, but the coefficient of the quadratic term is $O(\delta_i^3)$.

¹¹This is expected, as the extended MHD equations, which are mathematically equivalent to the two-fluid equations, are independent of \mathbf{E}_0 , but it is good to show it.

2.1.4 Incomplete Gyro-viscous Cancellation, No Diamagnetic Heat Flux

Computational models for the extended MHD equations often include the gyro-viscous stress but ignore the ion diamagnetic heat flux. We therefore consider the analytical solution of the two-fluid model with incomplete gyro-viscous cancellation and no diamagnetic heat flux. In this case, the dispersion relation to lowest order in ϵ and δ_i is

$$w^3 - \frac{1}{2}\alpha_z^2 \left(\beta_e + \frac{5}{3}\beta_i \right) w - \frac{1}{4}\alpha_y\alpha_z^2\beta_i \left(\beta_e + \frac{5}{3}\beta_i \right) \left(1 + \frac{1}{6}\beta_i \right) \delta_i \eta_i = 0 . \quad (48)$$

There is clearly the possibility of instability when $\beta_e = 0$, for then the constant term is $O(\beta_i^2) \gg O(\beta_i^3)$. The value of η_i^{crit} is

$$\eta_i^{crit} = 2\sqrt{2} \frac{\alpha_z \left(\beta_e + \frac{5}{3}\beta_i \right)^{1/2}}{\alpha_z \beta_i \left(1 + \frac{1}{6}\beta_i \right) \delta_i} , \quad (49)$$

which is minimum when $\beta_e = 0$. The properties of the system without diamagnetic heat flux are both quantitatively and qualitatively different than the properties when it is included.

2.1.5 No Gyro-viscosity, No Diamagnetic Heat Flux

For completeness, we also consider the case with neither gyro-viscosity nor diamagnetic heat flux. This corresponds to the Hall MHD model; it contains two-fluid effects but no FLR effects. The dispersion relation is a quadratic, whose solution at lowest order in ϵ and δ_i is

$$w^2 = \frac{1}{2}\alpha_z^2 \left(\beta_e + \frac{5}{3}\beta_i \right) \left[1 + \frac{3}{2}\alpha_y^2 \left(\beta_e + \frac{5}{3}\beta_i \right) \delta_i^2 \right] . \quad (50)$$

This is a *stable* parallel sound wave with two-fluid corrections at second order in δ_i . For the ITG-like mode, gyro-viscosity is *destabilizing*.

2.1.6 Properties of the Solutions

Here we discuss the similarities and differences between the the solutions of the three dispersion relations derived in Sections 2.1.2, 2.1.3, and 2.1.4. We use the specific parameters $B_0 = 2$ T, $n_0 = 2 \times 10^{20}$ / m³, $a = 1$ meter, $\alpha_y = 125.6$, and $\alpha_z = 0.1$ These result in $\delta_i = 0.0161$ and satisfy the ballooning ordering discussed in Section 1.1.

We first consider the values of η_i^{crit} given in Equations (44), (47) and (49). These are plotted in Figure 1 as functions of the electron temperature fraction

$f_e = \beta_e/(\beta_i + \beta_e)$ for the case $\beta = \beta_i + \beta_e = 0.05$. The blue curve (Curve 1) is Equation (44) (diamagnetic heat flux and complete gyro-viscous cancellation), the red curve (Curve 2) is Equation (47) (diamagnetic heat flux and incomplete gyro-viscous cancellation), and the gold curve (Curve 3) is Equation (49) (no diamagnetic heat flux and incomplete gyro-viscous cancellation). Curve 1 is infinite at $f_e = 0$, indicating complete stability when $\beta_e = 0$. Curve 2 is finite but large ($\eta_i^{crit} = 18.6$) in this limit, so that instability when $\beta_e = 0$ is possible but the threshold is large. (Recall that Curve 2 represents the most “physically realistic” case.) All three curves are infinite when $f_e = 1$ ($\beta_i = 0$) indicating stability when the ions are cold. Curves 1 and 2 are in agreement when $f_e > 0$. For these parameters, instability is most easily achieved when $f_e \sim 0.7$, or $T_{e0}/T_{i0} \sim 7/3$. The gyro-viscous cancellation is apparently an excellent approximation. Curve 3 (no diamagnetic heat flux) has completely different behavior: it is most unstable when $f_e = 0$ ($\beta_e = 0$), and is not even qualitatively similar to Curves 1 and 2 when $\beta_e > 0$. Clearly, the diamagnetic heat flux plays a crucial role in determining the stability of the system.

In Section 2.1.1 we showed that the solution of the cubic dispersion relation

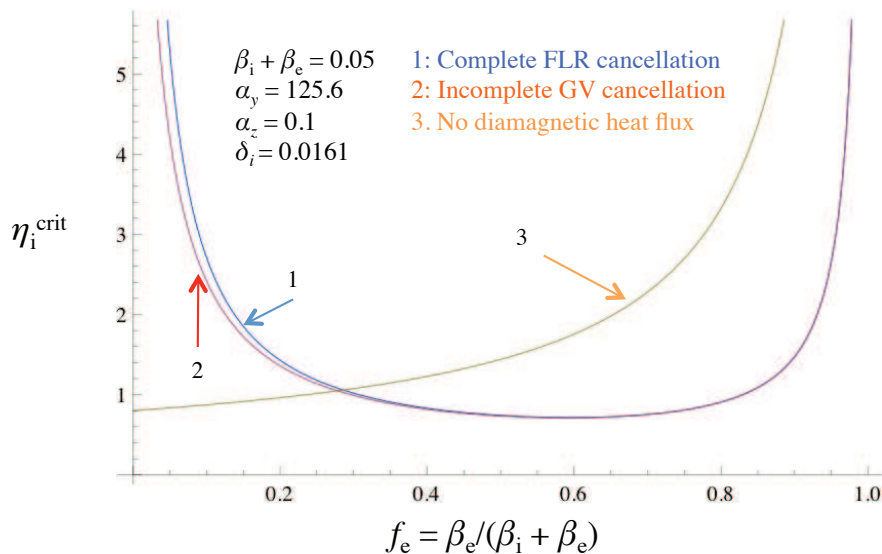


Figure 1: The instability criterion η_i^{crit} as a function of the electron β fraction for $\beta = \beta_e + \beta_i = 0.05$, $\alpha_y = 125.6$, $\alpha_z = 0.01$ and $\delta_i = 0.0161$. The blue curve assumes complete FLR cancellation (Section 2.1.2, Equation (44)); the red curve has incomplete gyro-viscous cancellation and complete diamagnetic heat cancellation (Section 2.1.3, Equation (47)); and, the gold curve has incomplete gyro-viscous cancellation and no diamagnetic heat flux (Section 2.1.4, Equation (49)). Curve 3 (gold) differs significantly from Curves 1 and 2, which are in good agreement.

$w^3 - 3Aw + B = 0$ is $w = \sqrt{A}(z + 1/z)$, where z is given by Equation (39). Both the growth rate of the instability and its real frequency can be written explicitly in terms of the coefficients for each of the dispersion relations (40), (46), and (48), but the expressions are complicated and again yield little insight. Instead, we consider the behavior of the growth rate as a function of η_i for the specific parameters of Figure 1, and for different values of the electron β fraction f_e . This is shown in Figure 2a-d where we plot the growth rate $\gamma = -Im(w)$ as a function of η_i for four different values of $f_e = \beta_e/(\beta_i + \beta_e)$. Except for the monotonic behavior, there is little similarity between Curves 1 and 2, and Curve 3.

The behavior of the roots of the dispersion relation for the “most realistic” case of Section 2.1.3 is illustrated in Figure 3. The blue curve is the locus of the roots of Equation (46) in the (η_i, w) plane for the case $\beta_i = 0.01$, $\beta_e = 0.04$ ($T_{e0}/T_{i0} = 4$), and the remaining parameters of this Section. Also shown for comparison is the Doppler shifted zero frequency mode, Equation (35) (with $\mathcal{E}_{x0} = -\beta_i^2 \eta_i/12$, as results at lowest order from reducing the dispersion relation to a deficient cubic),

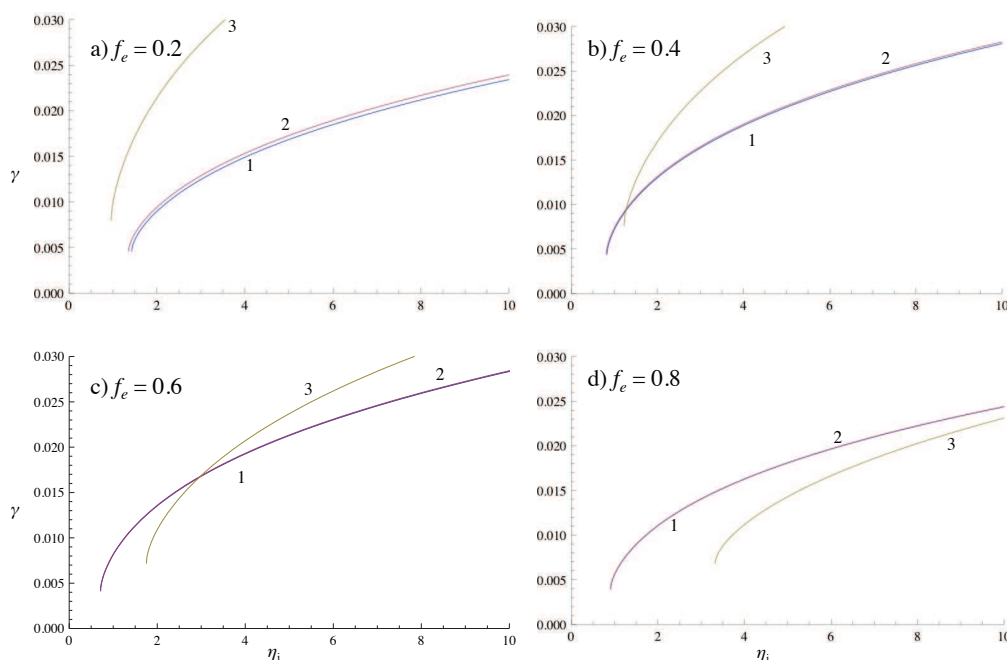


Figure 2: Growth rate of the electrostatic mode as a function of η_i for four different values of the electron β fraction: a) $f_e = 0.2$, b) $f_e = 0.4$. c) $f_e = 0.6$, and d) $f_e = 0.8$. In each case $\beta = \beta_i + \beta_e = 0.05$. The other parameters, and the labeling of the curves, is the same as in Figure 1. Curves 1 and 2 are almost identical except at low f_e .

and the “low frequency wave”

$$w = -\frac{1}{2}\alpha_y\beta_i\delta_i\eta_i\frac{\beta_e\left(1 + \frac{1}{6}\beta_i\right) + \frac{5}{18}\beta_i^2}{\beta_e + \frac{5}{3}\beta_i}, \quad (51)$$

which is obtained by equating the linear and constant terms in Equation (46). This has the appearance of a drift wave, but with a correction depending on β_e and β_i . When the medium is uniform ($\eta_i = 0$) this mode has zero frequency, and there two stable sound waves propagating in the $\pm z$ -directions (three real roots); these sound waves are indicated by the dots in the figure. When $-\eta_i^{crit} < \eta_i < \eta_i^{crit}$ (where η_i^{crit} is given by Equation (47)), there are three real roots: Equation (51), the low frequency drift-like mode, and the two sound waves modified by two-fluid and FLR effects. When $|\eta_i| > \eta_i^{crit}$ there is one real root and two complex conjugate roots, with the growth rate of the unstable mode given by Curve 2 in Figure 2d. It is tempting to interpret the onset of instability as an “interaction” between the sound wave and the drift-like wave when they have comparable frequency.

2.1.7 Dependence on $k_{\perp}\rho_i$

The validity of a fluid model of a plasma depends on the relative smallness of the ion gyro-radius, i.e., $k_{\perp}\rho_i \ll 1$. On the other hand, the important gyro-viscosity and ion diamagnetic heat flux terms only arise when $k_{\perp}\rho_i > 0$, i.e., the ion gyro-radius is small but finite. Using $k_{\perp}\rho_i = \alpha_y\delta_i\sqrt{\beta_i/2}$ we can eliminate α_y in terms of $k_{\perp}\rho_i$ at fixed β and density. The result is shown in Figure 4, where we plot the locus of the real roots of Equation (46) in the $(k_{\perp}\rho_i, w)$ plane for the parameters shown in the figure. There is a threshold value of $k_{\perp}\rho_i > 0.13$; below this value the system is stable, indicating the demonstrated stability in both Hall and ideal MHD; finite ion Larmor radius is necessary for instability. Whether $k_{\perp}\rho_i$ is simultaneously small enough for the validity of the fluid model awaits direct comparison with a kinetic solution using the same geometry, equilibrium, and parameters.

2.2 Electromagnetic Modes

We now consider electromagnetic modes, so that $\mathbf{E} = -\nabla\phi - \partial\mathbf{A}/\partial t$. Here we work in a reference frame in which the ions are stationary at $x = 0$, so that $E_{x0} = \beta_i\delta_i\eta_i/2$. (Of course, the electrons drift in the opposite direction.) The solvability equation has two large roots, $\omega^2 \gg \omega_A^2$. These are the perpendicular magneto-acoustic waves with $w^2 \sim \beta_i\alpha_y^2 \sim 1/\epsilon^4 \gg 1$. The low order (in ϵ) solvability condition $F_0(w) = 0$ is sixth order, and factors as

$$\left(w - \frac{1}{2}\alpha_y\beta_i\delta_i\eta_i\right)f_5(w) = 0. \quad (52)$$

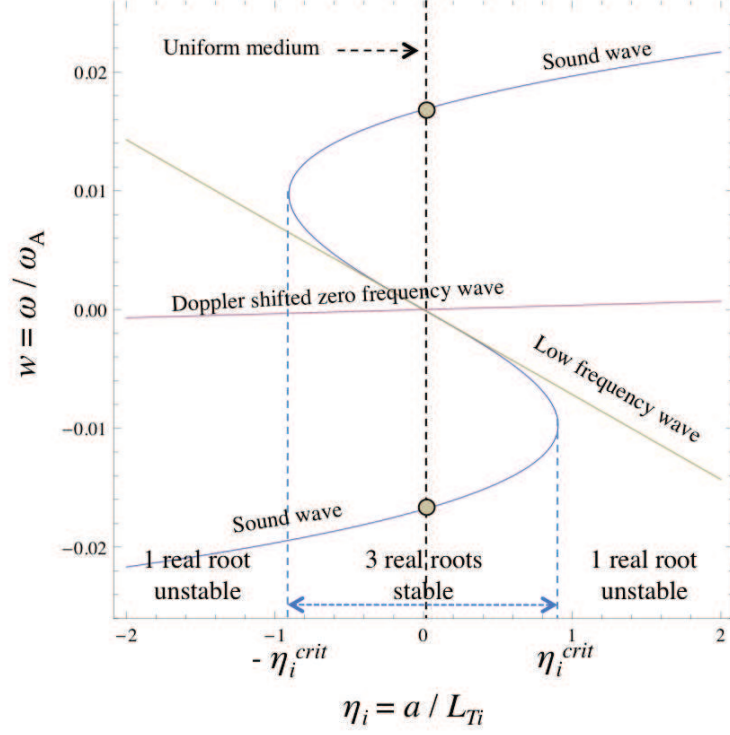


Figure 3: The locus of the roots of the dispersion relation with incomplete gyro-viscous cancellation and diamagnetic heat flux (Section 2.1.3) in the (η_i, w) plane for $\beta_i = 0.01$, $\beta_e = 0.04$ ($T_{e0}/T_{i0} = 4$), and the parameters of Figure 2. The red curve is the Doppler shifted zero frequency wave, Equation (35), the gold curve is the “low frequency” drift like wave, Equation (51), and the blue curve is the cubic dispersion relation, Equation (46). This cubic is has three real roots and is stable in the range $-\eta_i^{crit} < \eta_i < \eta_i^{crit}$; outside this range there is one real root and two complex conjugate roots, one if which is unstable with growth rate given in Figure 2d. The dots are the sound waves in a uniform medium.

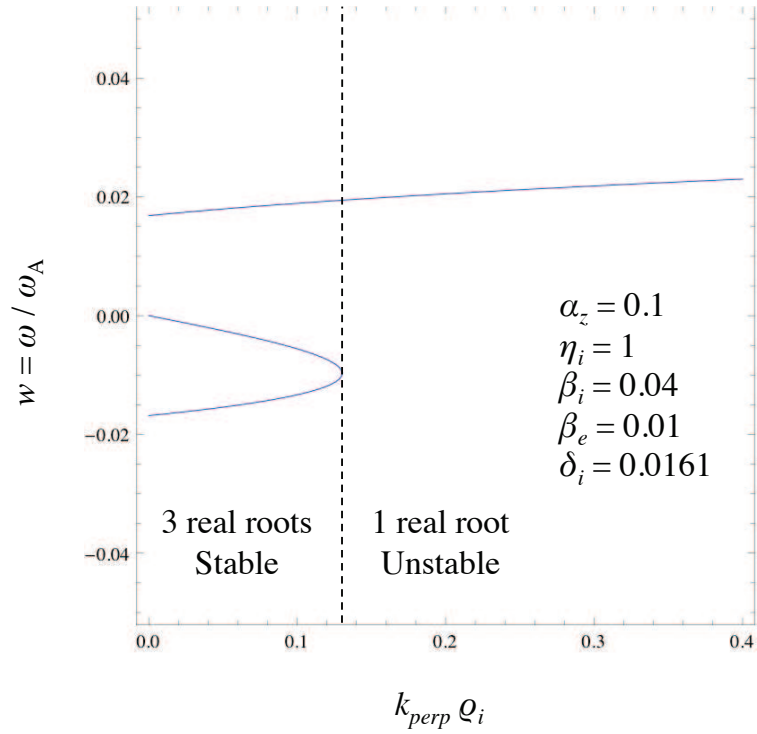


Figure 4: The locus of the roots of the Equation (46) in the $(k_{\perp}\rho_i, w)$ plane for $\beta_i = 0.01$, $\beta_e = 0.04$ ($T_{e0}/T_{i0} = 4$), and the parameters shown in the Figure. In this case, instability requires $k_{\perp}\rho_i > 0.13$.

The first factor appears as an ion drift wave, but is identical to the Doppler shifted zero frequency wave discussed in Section 2.1.1. The second is a quintic equation which has five roots: two shear Alfvén waves, two sound waves, and a low frequency wave similar to Equation (51).

The nature of the roots of the low order dispersion relation $f_5(w) = 0$ are illustrated¹² in Figure 6, including gyro-viscosity, diamagnetic heat flux, $\Gamma_e = 1$, and $n_0 = \text{constant}$, for the parameters of Section 2.1. The low frequency roots, including the drift wave (which in electrostatics appeared as the zero-frequency wave) have similar qualitative behavior to the electrostatic case, although the

¹²Solutions of equations of degree 5 or higher cannot be expressed in terms of radicals [7].

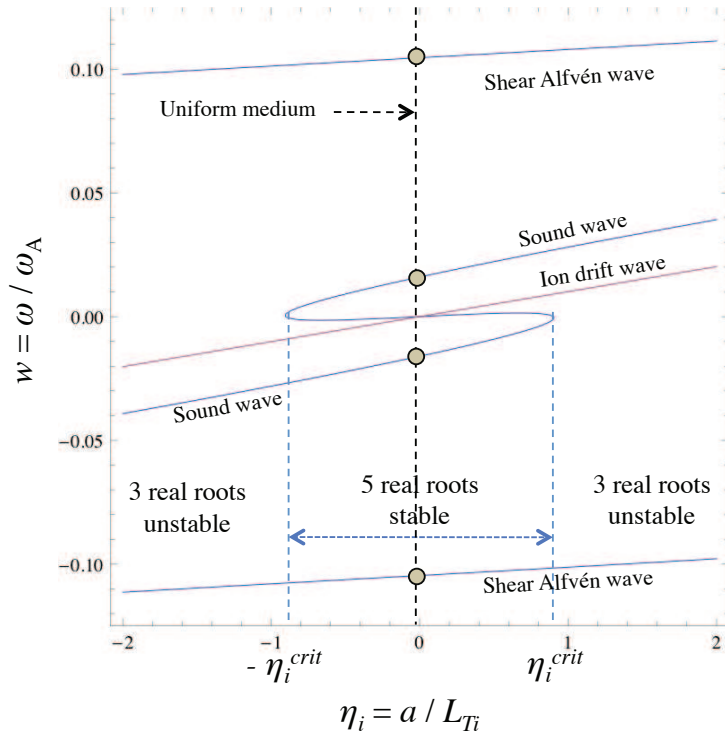


Figure 5: The locus of the roots of the electromagnetic dispersion relation with incomplete gyro-viscous cancellation and diamagnetic heat flux (Section 2.1.3) in the (η_i, w) plane for $\beta_i = 0.01$, $\beta_e = 0.04$ ($T_{e0}/T_{i0} = 4$), and the parameters of Figure 2. The red curve is the ion drift wave. The blue curve is the quintic dispersion relation, $f_5(w) = 0$. The quintic is has five real roots and is stable in the range $-\eta_i^{crit} < \eta_i < \eta_i^{crit}$; outside this range there are three real roots and two complex conjugate roots, one if which is unstable. The low frequency behavior is similar to the electrostatic case; however, the cubic dies not factor out algebraically. The dots are the Alfvén and sound waves in a uniform medium.

cubic behavior does not factor out of the quintic. The upper and lower branches are modified sound and magneto-acoustic waves. The remaining root is similar to the low frequency root given in Equation (51). The system is unstable when $|\eta_i| > \eta_{crit}$.

The electromagnetic mode is stable when $\beta_e \sim 0$. This is illustrated in Figure 6, where we plot the locus of the roots of the $f_5(w) = 0$ in the (f_e, w) plane for the parameters indicated in the figure, where $f_e = \beta_e/(\beta_i + \beta_e)$. There are five real roots when $f_e \rightarrow 0$ and $f_e \rightarrow 1$. There is an unstable root when $0.225 < f_e < 0.875$. The nature of the waves is indicated in the figure.

A comparison of the growth rate as a function of η_i for the electromagnetic (blue) and electrostatic (red) cases is shown in Figure 7. They are almost identical; the fluid ITG-like mode is essentially an electrostatic mode.

3 Local Solution of the Extended MHD Model

As noted in the beginning of Section 2, the electromagnetic two-fluid equations, Eqs. (18)-(25), are mathematically equivalent to the Extended MHD equations, Eqs. (3)-(7). While the analytic results of Sections 2.1 and 2.2 were obtained with the two-fluid model, NIMROD solves the Extended MHD equations, and it is instructive (and encouraging) to obtain the solutions of these equations directly.

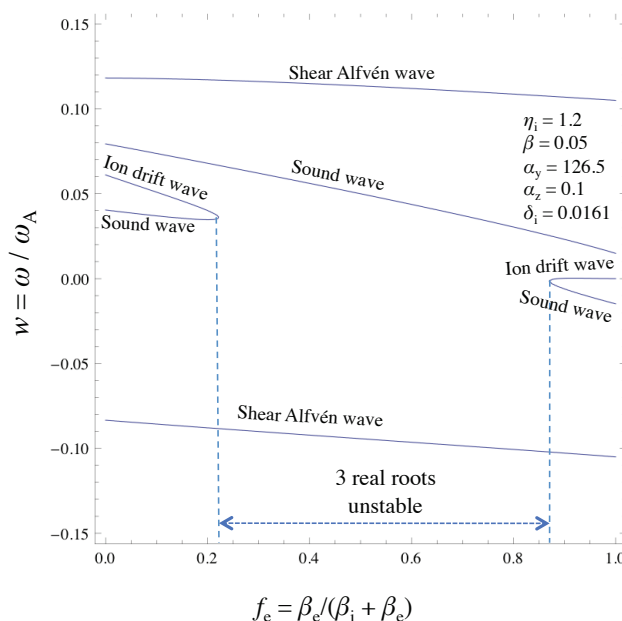


Figure 6: The roots of $f_5(w) = 0$ in the (f_e, w) plane, where $f_e = \beta_e/(\beta_i + \beta_e)$, for the parameters listed in the figure. The system is stable when $f_e \sim 0$ and $f_e \sim 1$.

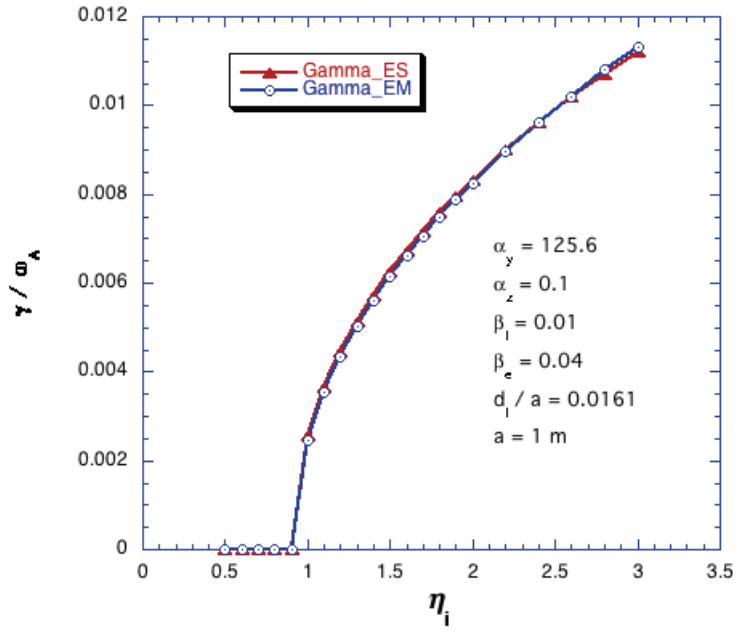


Figure 7: Comparison of the growth rate versus η_i for the electromagnetic (blue) and electrostatic (red) cases for $n_0 = \text{constant}$, $\Gamma_e = 1$, incomplete gyro-viscous cancellation, and diamagnetic heat flux.

The NIMROD code uses the temperature instead of the pressure as a dependent variable[17], so we seek solutions in this form, i.e., we replace p_s with nT_s wherever the pressure appears in the equations. This immediately presents a contradiction, since then the perturbed pressure $p_s(x) = n_0(x)T_s + T_{s0}(x)n$ is explicitly a function of x , which violates the local approximation. The consistent procedure is to evaluate the perturbed pressure at $x = 0$, so that in terms of the non-dimensional variables, $p_s = n + T_s$, which is now independent of x , and is in the spirit of the local approximation.

3.1 Ideal MHD and the Local Approximation

There is a detail that arises when using the local approximation to solve the Extended MHD equations. It stems from the requirement that the resulting solutions be compatible with the properties of *ideal* MHD. This is discussed below.

Ideal MHD is obtained from the Extended MHD model by setting $\delta_i = 0$, and it is well known that the equilibrium under consideration (n_0 and T_{e0} constant, and $T_{i0}(x)$) is stable in ideal MHD (i.e, $\delta W > 0$ for all displacements). However, setting $\delta_i = 0$ in the local approximation to the extended MHD equations yields an *unstable* mode, which is unphysical and indicates a breakdown in the model.

The origin of this unstable solution can be seen as follows. Consider the case with $\delta_i = 0$ (ideal MHD), $\alpha_y = 0$ (no perpendicular propagation), and the polarization $V_y = V_z = 0$ (the displacement is incompressible since V_x is constant). Then $n = 0$, and the remaining equations are

$$iwV_x - i\alpha_z B_x - \frac{1}{2}\eta_i\beta_i B_z = 0 , \quad (53)$$

$$iwB_x - i\alpha_z V_x = 0 , \quad (54)$$

$$iwB_z - \frac{1}{2}\eta_i\beta_i V_x = 0 . \quad (55)$$

These immediately yield the dispersion relation

$$w^2 = \alpha_z^2 - \frac{1}{4}(\eta_i\beta_i)^2 , \quad (56)$$

which is an exponentially growing mode if $(\eta_i\beta_i)^2 > 4\alpha_z^2$. It is an *unphysical* destabilization of the shear Alfvén wave in a non-uniform medium. This unstable mode is a result of the last terms in Equations (53) and (55), which come from the x -dependence of $\mathbf{J}_0(x) \times \mathbf{B}$ in the momentum equation, and $\nabla \times (\mathbf{V} \times \mathbf{B}_0(x))$ in the induction equation, respectively. When the the x -dependence of $\mathbf{B}_0(x)$ is ignored the system is stable for all η_i . This approximation is often used in analytical work[2, 3, 4, 5]. On the other hand, the limitation on the size of η_i

can be interpreted as a constraint for the validity of the local approximation: we should apply (or, perhaps more accurately, believe) the analysis only in cases where $-2\alpha_z/\beta_i \ll \eta_i \ll 2\alpha_z/\beta_i$, so that the system is robustly ideal MHD stable¹³. This is the approach we shall adopt. Then under these conditions the full (parallel, compressible) ideal MHD dispersion relation is

$$(\alpha_z^2 - w^2) \left[\alpha_z^2 - \frac{1}{4}(\eta_i\beta_i)^2 - w^2 \right] \left[\frac{1}{2}\alpha_z^2 \left(\beta_e + \frac{5}{3}\beta_i \right) - w^2 \right] = 0 . \quad (57)$$

The last term is a parallel sound wave, and the first term is the shear Alfvén wave. The middle term is a modification of the shear Alfvén wave; in a non-uniform medium it can become (unphysically) unstable if η_i^2 is large enough. Further, complete stability in a non-uniform medium is impossible when $\alpha_z = 0$,

When $\alpha_y \neq 0$ and no specific polarization is assumed, the ideal MHD dispersion relation in the local approximation is eighth order in w , so there are eight roots¹⁴. Two are the trivial roots $w = 0$, and the remaining six satisfy

$$\left[\alpha_z^2 - \frac{1}{4}(\eta_i\beta_i)^2 - w^2 \right] f_4(w) = 0 , \quad (58)$$

where $f_4(w)$ is the quartic (quadratic in w^2)

$$f_4(w) = \left(\frac{1}{2}\alpha_z^2\beta' - w^2 \right) (\alpha_z^2 - w^2) + \alpha_y^2 \left[\frac{1}{2}\alpha_z^2\beta' - \left(1 + \frac{1}{2}\beta' \right) w^2 \right] , \quad (59)$$

where $\beta' = \beta_e + (5/3)\beta_i$. The first factor in Equation (58) is a destabilization of the shear Alfvén branch. The roots of $f_4(w) = 0$ are always real and stable. They represent the coupling between the shear Alfvén branch and the magneto-sonic branch. When $\alpha_y = 0$, $f_4(w)$ reduces to the first and third terms in Equation (57).

The behavior in the (η_i, w) plane of the roots of the ideal MHD dispersion relation, Equation (58), are shown in Figure 8 for the parameters used in Sections 2.1 and 2.2. The vertical dashed line identifies the stable roots in a uniform medium: two “zero frequency” waves, two parallel sound waves, two shear Alfvén waves, and two magneto-sonic waves with $w^2 \gg 1$ (not shown). As $|\eta_i|$ increases the shear Alfvén frequency is modified, and the real roots for the mode disappear when $|\eta_i| = 2\alpha_z/\beta_i$ ($= 20$ for the given parameters). Above this value, one of the complex conjugate roots is unstable. The range of η_i for which the solution is a valid approximation is indicated by the shaded region.

Since the ideal MHD equations cannot be obtained *directly* from the electromagnetic two-fluid model (only the *limit* $\delta_i \rightarrow 0$ can be taken; see the discussion

¹³This can also be stated as an upper limit on the equilibrium ion temperature gradient: $T'_{0i} \ll (1/2)MV_A^2 k_z$; or the ion temperature, $T_{i0}/(MV_A^2/2) \ll k_z L_{Ti0}$.

¹⁴The extended MHD equations are ninth order, but when $\Gamma_e = 1$ the electron energy equation becomes $i\omega T_e = 0$, so $w = 0$ is the additional root.

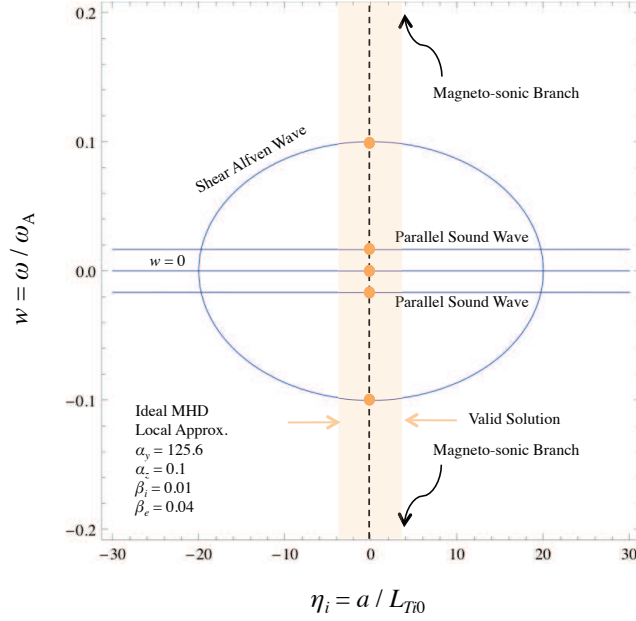


Figure 8: Roots of the ideal MHD dispersion relation in the local approximation, Equation (58), in the (η_i, w) plane. There are two stable magneto-sonic roots with $w^2 \sim \alpha_y^2 \gg 1$, as indicated. The remaining roots are the parallel sound waves, the shear Alfvén waves, and two trivial roots $w = 0$. The stable roots for a uniform medium ($\eta_i = 0$) are indicated. The shear Alfvén branch disappears for $|\eta_i| > 2\alpha_z/\beta_i = 20$ for these particular parameters, resulting in (unphysical) instability. The approximate region for physically valid solutions in the local approximation ($\eta_i^2 \ll 4\alpha_z^2/\beta_i^2$) is indicated by the shaded region.

following Equation (24)), the limitation on η_i was not considered in the analysis of that system. However, solutions outside the region where the ideal MHD system is stable (or when the dispersion of the shear Alfvén branch is significantly modified) should be viewed with suspicion. For the parameters used in the examples of Sections 2.1 and 2.2 (e.g., $\alpha_z = 0.1$, $\beta_i = 0.01$), the conditions for validity are $\alpha_z \neq 0$ and $|\eta_i| \ll 2\alpha_z/\beta_i = 20$, which are satisfied for all cases considered.

We remark that this instability is an artifact (or a limitation) of the local approximation. If the perturbations are allowed to vary with x , the simple algebraic system, Eqs. (53)-(55), becomes a differential system that always yields stable solutions. In particular, this mode will not arise in NIMROD calculations.

3.2 The Extended MHD Equations

We now proceed with the analytical solution of the Extended MHD equations, Eqs. (3)-(7), in the local approximation. The methodology is the same as described in Section 2, except we do not assume the ballooning ordering (i.e., $\epsilon = 1$).

A comparison of the locus of the roots of the local dispersion relation in the (w, η_i) plane for the two-fluid electrostatic, two-fluid electromagnetic, and Extended MHD models are shown in Figures 9-12 for four different cases: neither gyro-viscosity nor diamagnetic heat flux (Figure 9); gyro-viscosity but no diamagnetic heat flux (Figure 10); diamagnetic heat flux but no gyro-viscosity (Figure 11); and, both gyro-viscosity and diamagnetic heat flux (Figure 12). The remaining parameters are $\alpha_y = 125.6$, $\alpha_z = 0.1$, $\beta_i = 0.01$, $\beta_e = 0.04$, and $\delta_i = 0.0161$. In all cases where it is relevant, the gyro-viscous cancellations are incomplete. The region for validity in the local approximation ($\eta_i^2 \ll 4\alpha_z^2/\beta_i^2$) is indicated by the shaded region.

We first note that in all cases the solution of the two-fluid electromagnetic model is indistinguishable from that of the Extended MHD model. This is reassuring, as the two systems are mathematically equivalent.

Second, the dispersion properties of all the normal modes are significantly modified outside the region of validity. There are always only stable modes for a uniform medium ($\eta_i = 0$). In the first case (Figure 9), the diagonal line is an ion drift wave, and the sound waves form an ellipse that encircles the origin. Above $\eta_i = 10$ the roots for these modes become complex conjugates, with one of them unstable. This must be considered unphysical. The shear Alfvén branch becomes unstable when $|\eta_i| > 20$, which is residual behavior from the ideal MHD system discussed in Section 3.1. This is also unphysical.

Third, as shown in Figure 10 the effect of gyro-viscosity alone is to produce an interaction between the parallel sound waves and the perpendicular ion drift wave. This results in the “S” shaped curve near the origin; the “middle” of the “S” is all that remains of the drift wave. This entire distortion occurs within the region

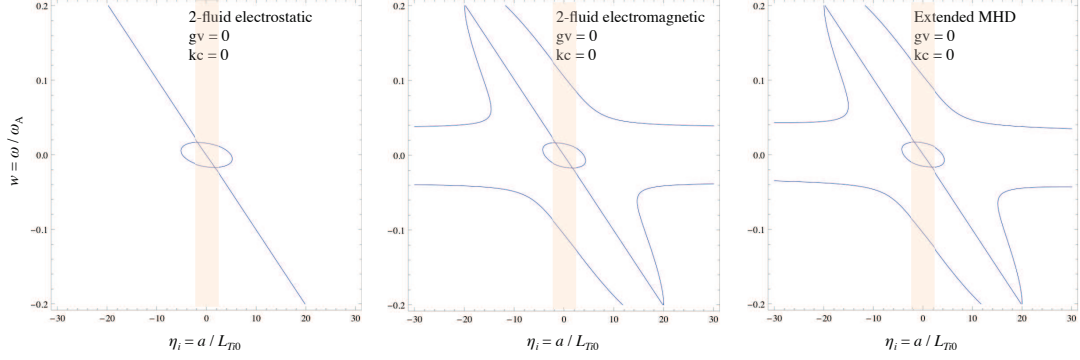


Figure 9: Roots of the unordered dispersion relation for the two-fluid electrostatic model (left), two-fluid electromagnetic model (center), and the Extended MHD model (right), in the (η_i, w) plane. The figure contrasts the properties of the three models, and illustrates the excellent agreement between the two-fluid electromagnetic model and Extended MHD; the latter are mathematically equivalent. There is neither gyroviscosity nor diamagnetic heat flux. The remaining parameters are $\alpha_y = 125.6$, $\alpha_z = 0.1$, $\beta_i = 0.01$, $\beta_e = 0.04$, and $\delta_i = 0.0161$. The diagonal line is the ion drift wave. The approximate region for physically valid solutions in the local approximation ($\eta_i^2 \ll 4\alpha_z^2/\beta_i^2$) is indicated by the shaded region. For a uniform medium ($\eta_i = 0$) there are seven stable waves: a zero frequency wave (which becomes the drift wave when $\eta_i \neq 0$), two sound waves (the ellipsoid), two shear Alfvén waves, and two magneto-sonic waves with $w^2 \gg 1$ (not shown). The sound waves become unstable for $|\eta_i| > 6$. The shear Alfvén waves become unstable for $|\eta_i| > 20$; this is an artifact of the underlying MHD instability. All unstable modes lie outside the region of validity, and are unphysical.

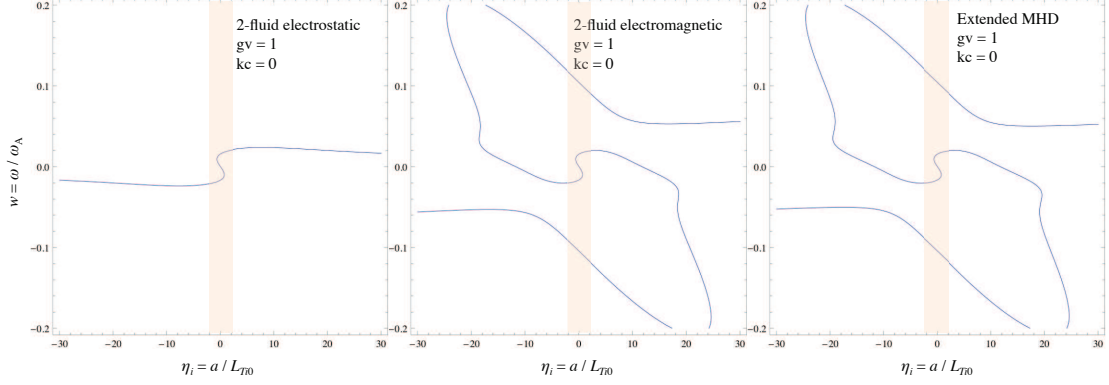


Figure 10: The same as Figure 9, except with gyro-viscosity but not diamagnetic heat flux. The “S” curve in the center is the result of FLR modification of the drift wave and parallel sound waves; the “middle” of the “S” is all that remains of the drift wave. The loss of real roots at $|\eta_i| \sim 1$ is the onset of the ITG-like mode. The dispersion properties of both the sound and shear Alfvén waves is evident for $\eta_i^2 \gg 1$, as is the residual (ideal MHD) destabilization of the Alfvén wave for $|\eta_i| > 20$. These effects are unphysical. The approximate region for physically valid solutions in the local approximation ($\eta_i^2 \ll 4\alpha_z^2/\beta_i^2$) is indicated by the shaded region.

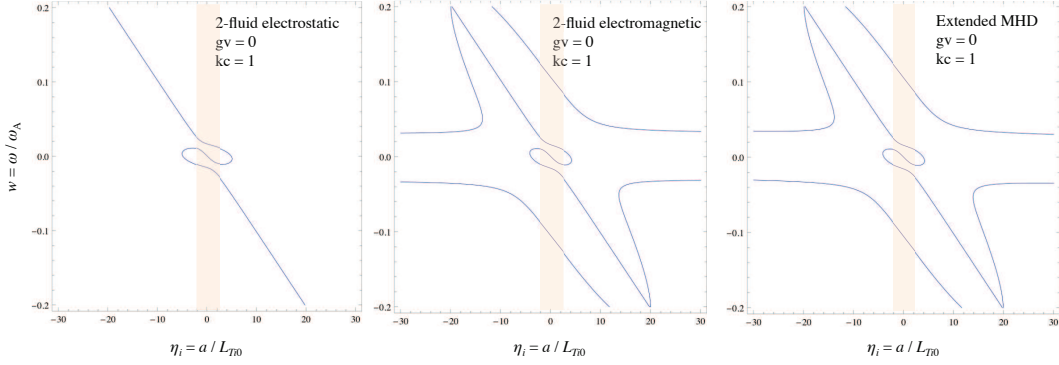


Figure 11: The same as Figure 9, except with diamagnetic heat flux but not gyroviscosity. The effect of diamagnetic heat flux alone is to “mix up” the sound and drift waves at low frequency and small $|\eta_i|$. The approximate region for physically valid solutions in the local approximation ($\eta_i^2 \ll 4\alpha_z^2/\beta_i^2$) is indicated by the shaded region. Note that there are only real roots in this region, so the system remains stable when the local approximation is valid.

of validity, so the onset of unstable roots near $|\eta_i| \sim 1$ is physical and is the onset of the ITG-like instability discussed in Sections 2.1 and 2.2. The sound and shear Alfvén branches unphysically merge and disappear near $|\eta_i| \sim 20$. This is residual behavior from the unphysical destabilization of the shear Alfvén branch in ideal MHD.

Fourth, the effect of diamagnetic heat flux alone is shown in Figure 11. Again there is an interaction between the drift wave and the parallel sound waves, but the loss of real roots occurs outside the region of validity. There are always three real roots when the local approximation is valid.

Finally, the combined effects of gyro-viscosity and diamagnetic heat flux are shown in Figure 12. For these parameters (i.e., $\beta_i = 0.01$, $\beta_e = 0.04$), the behavior of the low frequency roots is identical in all three models. Of course, in Section 2.1.6 we showed that both gyro-viscosity and diamagnetic heat flux are required to prevent ITG-like instability when $\beta_e \rightarrow 0$.

4 Accounting for Approximate x -dependence of the Perturbations

The calculations of the previous sections used the local approximation, i.e., the dependence of the perturbations was assumed to be $f(x, y, z, t) = \tilde{f} e^{i\omega t + ik_y y + ik_z z}$; the perturbations are independent of x . This reduces the problem to algebra. We have also used the ballooning ordering $k_y : k_z : 1/L_{Ti0} :: 1/\epsilon^2 : 1 : 1$, with $\epsilon \ll 1$, and have generally found the dispersion properties of the system to lowest order

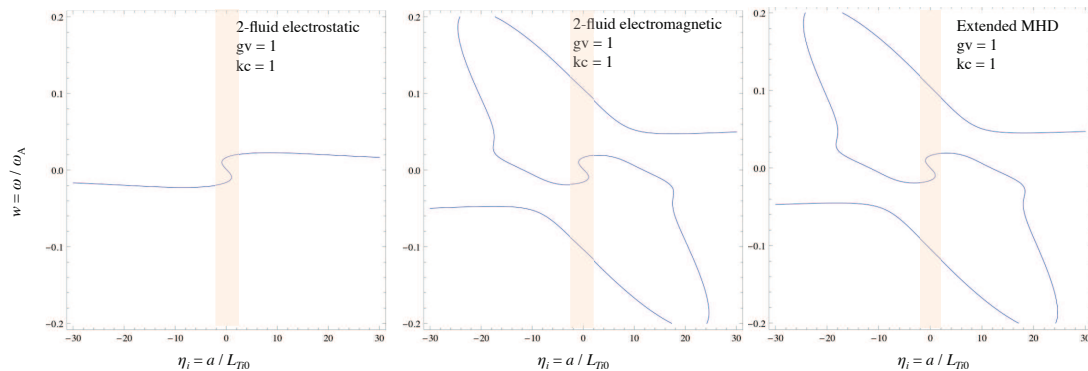


Figure 12: The same as Figure 9 , except with both gyro-viscosity and diamagnetic heat flux. The results are indistinguishable from Figure 10, indicating that gyro-viscosity is the dominant effect for these parameters. The approximate region for physically valid solutions in the local approximation ($\eta_i^2 \ll 4\alpha_z^2/\beta_i^2$) is indicated by the shaded region.

in ϵ . Of course, the results only have physical significance when $k_{\perp}\rho_i \ll 1$, as this is the assumption used to derive the gyro-viscous and diamagnetic heat flux closures.

Recently Hegna[18] and Sovinec[19] have considered the electrostatic case with both equilibrium density, $n_0(x) = n_0 e^{x/L_n}$, and ion temperature, $T_{i0}(x) = T_{i0} e^{x/L_{T_{i0}}}$, varying in x (but $T_{e0} = \text{constant}$). These calculations contain (apparently) arbitrary x -dependence of the perturbations and yet result in purely algebraic dispersion relations. In a frame where $\mathbf{E}_0 = 0$, Hegna's result [18] is the cubic

$$\omega^3 - \omega_{*e}\omega^2 - k_{\parallel}^2 \frac{T_{e0} + \frac{5}{3}T_{i0}}{M} \omega - k_{\parallel}^2 \frac{T_{e0}}{M} \omega_{*i} \left(\frac{2}{3} - \eta_i \right) = 0, \quad (60)$$

where $\omega_{*i} \equiv (k_{\perp}T_{i0}/eB_0)(n'_0/n_0)$, $\omega_{*e} \equiv -(T_{e0}/T_{i0})\omega_{*i}$, and $\eta_i \equiv d \ln T_{i0}/d \ln n_0 \equiv L_n/L_{T_{i0}}$. (Note that this definition of η_i differs from that used in most of this work, where we have assumed $n_0 = \text{constant}$, so $L_n = \infty$; then in Hegna's definition, $\eta_i = \infty$ also.) Hegna states that "in the low- k_{\parallel} limit" one can balance the quadratic term with the constant term" and obtain $\omega^2 = k_{\parallel}^2(T_{i0}/M)(2/3 - \eta_i)$, which is unstable for $\eta_i > 2/3$.

In our non-dimensional variables (*but now measuring length in units of L_n*), we have $n_0(x) = e^x$, $T_{i0}(x) = e^{\eta_i x}$, and Equation (60) becomes

$$w^3 + \frac{1}{2}\alpha_y\beta_e\delta_i w^2 - \frac{1}{2}\alpha_z^2 \left(\beta_e + \frac{5}{3}\beta_i \right) w - \frac{1}{8}\alpha_y\alpha_z^2\beta_i\beta_e\delta_i \left(\frac{2}{3} - \eta_i \right) = 0. \quad (61)$$

We can extend the analysis of the previous sections to include an approximate x -dependence of the perturbations, i.e, we assume $f(x) \simeq \tilde{f}e^{i\alpha_x x}$. This would be an exact Fourier representation if the equilibrium had no x -dependence, and the system was periodic in that dimension. It may be a *decent approximation* if the equilibrium varies only slowly in x , i.e., $\lambda_x \ll L_n, L_{T_{i0}}$. However, we should also require $\lambda_y \ll \lambda_x$. A consistent ordering of the non-dimensional variables is $\alpha_x : \alpha_y : \alpha_z : 1/L :: 1/\epsilon : 1/\epsilon^2 : 1 : 1$.

We introduce this *ansatz* and ordering into the electrostatic equations and, as before, determine dispersion relation by setting the determinant of the system to zero and retaining terms that are only lowest order in ϵ . To be consistent with Hegna's calculation, we have also set $\mathbf{E}_0 = 0$. It is reassuring that the result is not only independent of α_x , but to lowest order in ϵ and δ_i *it is identical to the result with $\alpha_x = 0$* (i.e., the local approximation). The result is a cubic of the form

$$w^3 + a_2 w^2 + a_1 w + a_0 = 0, \quad (62)$$

where

$$a_2 = -\frac{1}{2}\alpha_y\delta_i \left\{ \beta_e \left(1 + \frac{4}{3}\beta_i \right) + \beta_i \left[1 - \eta_i + \frac{4}{3}\beta_i (1 + \eta_i) \right] \right\}, \quad (63)$$

$$a_1 = -\frac{1}{2}\alpha_z^2 \left(\beta_e + \frac{5}{3}\beta_i \right) , \quad (64)$$

and

$$a_0 = \frac{1}{4}\alpha_y\alpha_z^2\beta_i\delta_i\left\{\beta_e\left(\frac{2}{3}-\eta_i\right)+\frac{5}{6}\left[\beta_i(2+\eta_i)+\beta_e^2+\beta_i^2(1+\eta_i)\right]\right\} . \quad (65)$$

With the exception of a_1 , there is only superficial resemblance between the coefficient of Equations (61) and (62).

It is physically relevant to compare the solutions of Equations (61) and (62) in the regime $k_\perp\rho_i = \alpha_y\delta_i\sqrt{\beta_i/2} \ll 1$. Using this expression to eliminate α_y in terms of $k_\perp\rho_i$, Equation (61) is

$$w^3 + \frac{\beta_e}{\sqrt{\beta_i}}(k_\perp\rho_i)w^2 - \frac{1}{2}\alpha_z^2\left(\beta_e + \frac{5}{3}\beta_i\right)w - \frac{1}{8}\alpha_z^2\beta_e\sqrt{\beta_i}\left(\frac{2}{3}-\eta_i\right)(k_\perp\rho_i) = 0 . \quad (66)$$

It is now clear that a consistent limit for balancing the quadratic and constant terms is $k_\perp\rho_i \ll 1$, yielding instability when $\eta_i > 2/3$. (Balancing the cubic and linear terms yields parallel sound waves.) The coefficients of Equation (62) become

$$a_2 = -\frac{\beta_e\left(1+\frac{4}{3}\beta_i\right)+\beta_i\left[1-\eta_i+\frac{4}{3}\beta_i(1+\eta_i)\right]}{\sqrt{\beta_i}}(k_\perp\rho_i) , \quad (67)$$

$$a_1 = -\frac{1}{2}\alpha_z^2\left(\beta_e + \frac{5}{3}\beta_i\right) , \quad (68)$$

and

$$a_0 = \frac{1}{2}\alpha_z^2\sqrt{\beta_i}\left\{\beta_e\left(\frac{2}{3}-\eta_i\right)+\frac{5}{6}\left[\beta_e\beta_i(2+\eta_i)+\beta_e^2+\beta_i^2(1+\eta_i)\right]\right\}(k_\perp\rho_i) . \quad (69)$$

The marginal stability points for Equations (61) and (62) can be determined by examining their discriminants. For a cubic of the form $aw^3 + bw^2 + cw + d = 0$, the discriminant is

$$\Delta = 18abcd - 4b^3d + b^2c^2 - 4ac^3 - 27a^2d^2 . \quad (70)$$

If $\Delta > 0$ there are three real, distinct roots and the solution is stable. If $\Delta < 0$ there is one real root and two complex conjugate roots; the system is unstable. The boundary between stable and unstable solutions is $\Delta = 0$, for which there are three real roots, two of which are equal.

The locus of the curves $\Delta = 0$ for Equations (61) (Blue) and (62) (Red) in the $(\eta_i, k_\perp\rho_i)$ plane are shown Figure 13. The upper right of the figure is unstable, and the lower left and bottom are stable. Equation (61) becomes unstable at $\eta_i = 2/3$ only for $k_\perp\rho_i \sim 1$; in this limit the critical value for Equation (62) is slightly

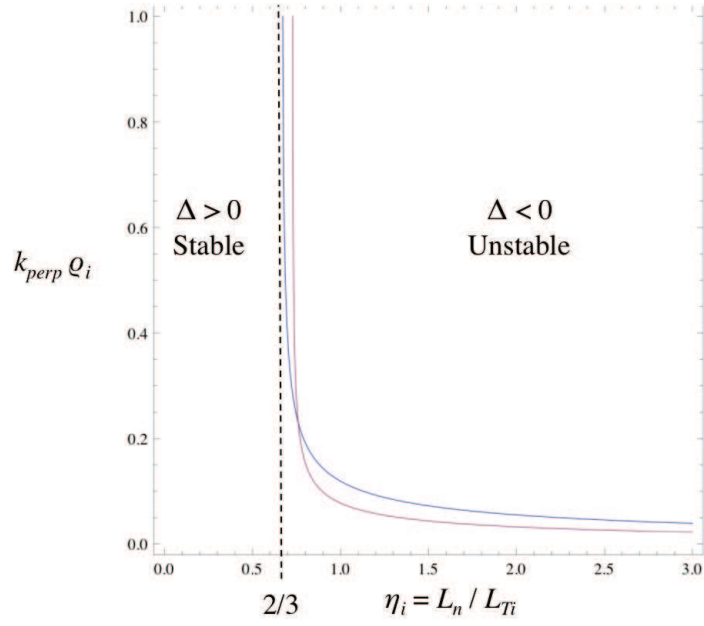


Figure 13: Locus of the discriminant equation $\Delta = 0$ for Equations (66) (Blue) and (62) (Red) in the $(\eta_i, k_{\perp} \rho_i)$ plane. Equation (66) asymptotes to $\eta_i = 2/3$ only for $k_{\perp} \rho_i \sim 1$; Equation (62) asymptotes to a slightly larger value, $\eta_i \sim 0.7$. The closures used in the equations are only physically valid when $k_{\perp} \rho_i \ll 1$.

larger, $\eta_i \sim 0.7$. However, the equations are only physically valid for $k_{\perp}\rho_i \ll 1$. In that regime, instability with Equation (61) requires a slightly larger value of $k_{\perp}\rho_i$ for a given η_i , and a considerably larger value of η_i for a given value of $k_{\perp}\rho_i$. Nonetheless, the overall behavior of the solutions of the equations is remarkably similar.

5 Effects of Gravity

In Section 1, we contrasted the ITG-like mode and the g -mode. The ITG-like mode requires two-fluid/FLR effects and finite parallel wave number for instability, while the g -mode is *unstable* in two-dimensional ideal MHD and is *stabilized* by two fluid and/or FLR effects.

In this section we briefly discuss the the g -mode in the context of the same theory that we have used for the ITG-like mode. We reproduce quantitatively the well-known properties of the $\beta = 0$ g -mode[24], but we find some interesting differences when $\beta > 0$. We speculate that these differences are related to a distinction between “compressibility” and “finite- β effects”.

We also present results that combine the effects of gravitational acceleration with the previously discussed theory of the ITG-like mode. We find, not surprisingly, that the effect of increasing gravity is to destabilize eventually the combined three-dimensional two-fluid/FLR system, even with $\eta_i = 0$.

This combined system will not be studied computationally. In that sense, this section, like Section 4, stands alone.

5.1 Equilibrium

So far, we have considered only the simple case when the magnetic field lines are straight and parallel; they have no curvature. We now briefly consider an extension to this equilibrium that *approximates* the effects of curved field lines. The condition for force balance when the magnetic field lines have curvature (i.e., are not straight) is

$$\nabla \left(\frac{B^2}{2\mu_0} + p_e + p_i \right) = \frac{B_0^2}{2\mu_0} \mathbf{K} , \quad (71)$$

where $\mathbf{K} = -\hat{\mathbf{b}} \times (\nabla \times \hat{\mathbf{b}})$ is the field line curvature. For the case of a straight field line, this force is can be approximated as a gravitational acceleration \mathbf{g} perpendicular to \mathbf{B} , i.e.,

$$\nabla \left(\frac{B^2}{2\mu_0} + p_e + p_i \right) = Mn_0 \mathbf{g} . \quad (72)$$

This approximation is often used as a proxy for the effects field line curvature even when the field lines are straight, as is the case for all equilibria considered here. However, the analogy is not exact as the gravitational acceleration \mathbf{g} in Equation (72) is assumed to be uniform, whereas the force on the right hand side of Equation (71) depends on the local value of \mathbf{B} .

We will consider the case when $\mathbf{g} = -g\hat{\mathbf{e}}_x$; g can be either positive or negative. We assume the equilibrium density varies as $n_0(x) = n_0 e^{x/L_{n0}}$. Using the scale length $a = L_{n0}$, Equation (72) in non-dimensional variables is

$$\frac{d}{dx} \left(B_0^2 + \beta_i p_i + \beta_e p_e \right) = -2w_g^2 n_0(x) , \quad (73)$$

where now $n_0(x) = e^x$ and $w_g^2 = \omega_g^2/\omega_A^2$, and $\omega_g^2 = g/L_{n0}$ is the characteristic gravitational frequency¹⁵. The non-dimensional equilibrium magnetic field is found by integrating Equation (73) from 0 to x .

The drift velocity is

$$V_{iy0}(x) = -\frac{E_{x0}}{B_0(x)} + \frac{\beta_i \delta_i \eta_i}{2B_0(x)} e^{\eta_i x} + \frac{w_g^2 \delta_i}{B_0(x)} . \quad (74)$$

The last term is an additional gravitational drift arising from $\mathbf{B}_0 \times \mathbf{g}$. The density dependence has been cancelled; it does not depend on β_i . The electrons do not experience this drift since $m_e = 0$.

Since we are measuring length in units of L_{n0} , the non-dimensional ion temperature profile is $T_{i0} = e^{\eta_i x}$, where $\eta_i = L_{n0}/L_{Ti0}$, and the ion pressure profile is $p_{i0} = e^{(1+\eta_i)x}$.

The equation for the perturbed ion velocity, Equation (20), gains an additional term proportional to the perturbed density, $w_g^2 \delta_i n$.

We investigate the effect of the additional equilibrium force and drift on ITG-like modes using the two-fluid electro-magnetic model, the local approximation, and the ballooning ordering (see Section 2.2); we must order $w_g^2 \sim \epsilon^2$ to keep the drifts in balance. The formalism is the same: find the determinant of the algebraic system, set it to zero, retain terms that are lowest order in ϵ , and examine the properties of the roots of this dispersion relation.

We first consider briefly the properties of the system with gravity when the equilibrium ion temperature is spatially uniform, $\eta_i = 0$.

¹⁵Note that in our model w_g^2 can be either positive or negative.

5.2 The Gravitational Interchange Mode with Uniform Ion Temperature

5.2.1 $\beta = 0$

It is well known that the cold, electro-static, two-dimensional system with $\alpha_z = \eta_i = \beta_i = \beta_e = 0$ described above (a stratified fluid) can be unstable in both hydrodynamics[23] and ideal MHD[24]. In both cases the dispersion relation in the local approximation is

$$w^2 = -w_g^2, \quad (75)$$

so that the system is unstable with growth rate¹⁶ $\gamma_{MHD} = \sqrt{g/L_{n0}}$ if $\omega_g^2 > 0$. This instability is commonly called the g -mode. The incompressible ideal MHD energy principle for this system with density $\rho = Mn_0(x)$ is[25]

$$\delta W = \frac{1}{2} \int g \frac{d\rho}{dx} \xi_x^2 dx, \quad (76)$$

so that $\delta W < 0$ and the system is unstable if g and $d\rho/dx$ have opposite signs¹⁷. When two-fluid effects are included (i.e., $\delta_i > 0$) the local dispersion relation is of the form[24]

$$w(w - w_*) + w_g^2 = 0, \quad (77)$$

where $w_* = \alpha_y V_{yi0}(0)$ is the normalized drift frequency. The system becomes stable when $w_*^2 > 4w_g^2$, or $\omega_* > 2\gamma_{MHD}$. This mode is *electro-static*; it does not perturb the magnetic field.

In the local approximation and ballooning ordering, the *electro-magnetic* dispersion relation with $\alpha_z = \beta_i = \beta_e = \eta_i = 0$, but $\delta_i > 0$ (including two-fluid effects), at lowest order in ϵ is a cubic¹⁸ in w that can be factored as

$$(w - \alpha_y \delta_i w_g^2) [w(w - \alpha_y \delta_i w_g^2) + w_g^2] = 0. \quad (78)$$

The first term is a ‘‘gravitational drift wave’’, and the second term is in the form of Equation (77) with $w_* = \alpha_y \delta_i w_g^2$; this is the gravitational drift frequency corresponding to the last term in Equation (74). It has the proper stabilizing effect; we remark that the non-dimensional stabilization condition can be written as $\alpha_y^2 \delta_i^2 w_g^2 / 4 > 1$. When $\delta_i \rightarrow 0$ we obtain the ideal MHD result of Equation (75).

¹⁶Remember that in our case $g > 0$ means that \mathbf{g} is in the *negative* x -direction, and $L_{n0} > 0$ means that the density gradient is in the *positive* x -direction. The growth rate is independent of α_y only for $\alpha_y \gg 1$, as is the case here.

¹⁷When compressibility is included it is possible to have instability when $gd\rho/dx > 0$ as long as it is not too large[25]. But, see Section 5.2.2

¹⁸Two additional magneto-acoustic waves appear only at higher order in ϵ .

We now consider the three-dimensional case with $\alpha_z > 0$ but still $\ll \alpha_y$. This introduces the shear Alfvén wave that may provide stabilization through field line bending. With $\delta_i \rightarrow 0$ the ideal MHD dispersion relation is a quadratic in w^2 ,

$$w^4 - (\alpha_z^2 - w_g^2) w^2 - \alpha_z^2 w_g^4 = 0. \quad (79)$$

The solution is

$$2w_{\pm}^2 = \alpha_z^2 - w_g^2 \pm \sqrt{(\alpha_z^2 - w_g^2)^2 + 4\alpha_z^2 w_g^4}. \quad (80)$$

When $\alpha_z = 0$ this gives usual g -mode, and when $w_g^2 = 0$ it yields the parallel shear Alfvén wave. When both are non-zero, stability requires $w_{\pm}^2 > 0$. The last term in Equation (79), $-\alpha_z^2 w_g^4 < 0$, is the product of the roots w_+^2 and w_-^2 ; it is negative. This means that one of the roots is always negative and unstable. Therefore, to within the accuracy of our approximations, *the ideal MHD g -mode with $\beta = 0$ cannot be stabilized by finite parallel wave number.*

When $\delta_i > 0$ (two-fluid), but $\beta_i = \beta_e = \eta_i = 0$, the dispersion relation is the *full* quartic

$$w^4 - 2\alpha_y \delta_i w_g^2 w^3 + [w_g^2 (1 + \alpha_y^2 \delta_i^2 w_g^2) - \alpha_z^2] w^2 - \alpha_y \delta_i w_g^2 w - \alpha_z^2 w_g^4 = 0. \quad (81)$$

This equation is sufficiently complicated that we resort to graphical analysis for specific parameters. The loci of the roots of Equation (81) in the (δ_i, w) plane are shown in Figure 14 for the given parameters. For these parameters, the 2-fluid g -mode in a *cold plasma* (i.e., $\beta = 0$) is stabilized for $\delta_i > 0.1$. The effect of finite parallel wave number is illustrated in Figure 15, where we plot the locus of the roots of Equation (81) in the (α_z, w) plane for four different values of δ_i . For these parameters there are only two real roots, and there is no indication of stabilization by finite α_z . This suggests, but does not prove, that the two-fluid g -mode in a cold plasma may not be stabilized by finite α_z within the constraints of the local approximation and ballooning ordering. Apparently the field line bending energy due to finite parallel wave number appears at higher order in ϵ .

The classical analysis of the g -mode in a magnetized fluid is carried out in the electro-static approximation, $\nabla \times \mathbf{E} = 0$, which is referred to as the “low- β ” approximation[24]. The equilibrium magnetic field is “approximately constant”, as is the equilibrium temperature, and the ion Larmor radius is taken to be finite. The equilibrium pressure variation is entirely due to the density variation. This allows the analysis to include the effects of the gyro-viscous stress tensor. There are two stabilizing effects, one due to the extended MHD Ohm’s law (what we have called “two-fluid effects”), and the other due to the finite ion Larmor radius (what we have called “FLR effects”). They enter the results in exactly the same way [i.e., they lead to a dispersion relation with the form of Equation (77)], and their effects are additive. This is not surprising since the stabilizing effect derives

the equilibrium drift velocity, so any terms that produce a drift can also provide stabilization.

In our model the gyro-viscosity enters the ion momentum equation, and the diamagnetic heat flux enters the ion energy equation, with a coefficient proportional to $\delta_i \beta_i$ [see Equation (20)]. The electron pressure enters the extended Ohms law, Equation (21), with a coefficient proportional to $\delta_i \beta_e$. With $\beta_i = \beta_e = 0$, the g -mode stabilization described above is entirely due to ‘‘Hall effects’’, the term $\mathbf{V}_e \times \mathbf{B}$ in the electron equation of motion. The results are completely consistent with Ref. [24], but do not describe FLR effects.

Further, it has been shown[26] that, when finite β is considered, ‘‘complete...stabilization [of the g -mode] may not be attainable by ion gyro-viscosity or two-fluid effect alone in the framework of extended MHD’’. We are therefore motivated to consider solutions with both β_i and β_e greater than zero, but $\eta_i = 0$.

5.2.2 $\beta > 0$

We first consider the ideal MHD case $\delta_i \rightarrow 0$ with $\eta_i = \alpha_z = 0$, $\beta_i > 0$, and $\beta_e > 0$. The low order dispersion relation is

$$w^2 = -w_g^2 + F(\beta_i, \beta_e) , \quad (82)$$

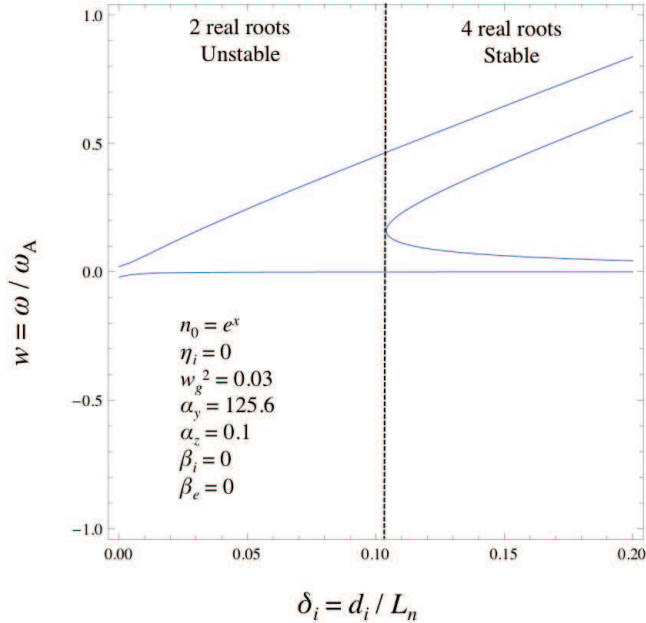


Figure 14: Locus of the roots of Equation (81) in the (δ_i, w) plane for the given parameters. This illustrates 2-fluid stabilization of the three dimensional $\beta = 0$ g -mode when $\alpha_z > 0$. For these parameters, the system becomes stable when $\delta_i > 0.1$.

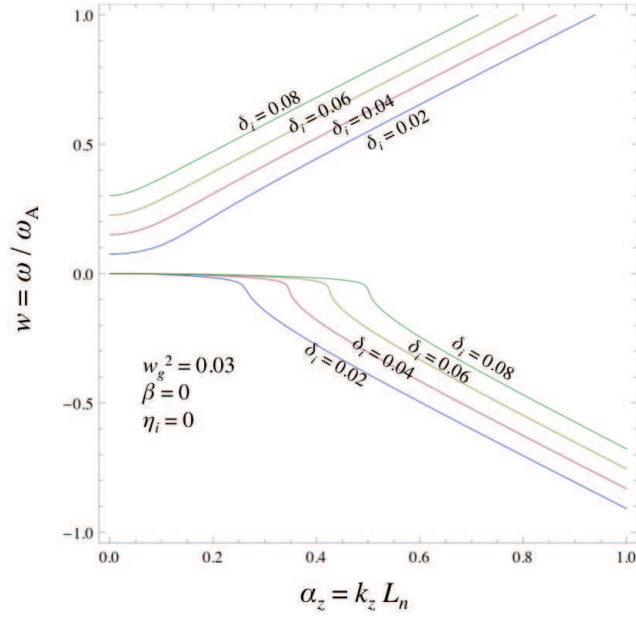


Figure 15: Locus of the roots of Equation (81) in the (α_z, w) plane for four different values of δ_i in the range $0.02 \leq \delta_i \leq 0.08$. There are only two real roots for $0 \leq \alpha_z \leq 1$, so the system is unstable. There is no indication of stabilization by finite α_z for these parameters.

where

$$F(\beta_i, \beta_e) = \frac{1}{2} \frac{\beta \left(1 - \frac{1}{2}\beta\right)}{1 + \frac{1}{2} \left(\beta_e + \frac{5}{3}\beta_i\right)}, \quad (83)$$

and $\beta = \beta_e + \beta_i$. The additional term is *stabilizing* if $\beta < 2$. The condition for stability is $F(\beta_i, \beta_e) > w_g^2 > 0$. This means that an unstable two-dimensional g -mode can be stabilized with sufficient β , provided $\beta < 2$. Conversely, a finite- β system (no matter how small the value of β , but with $\beta < 2$) requires that the condition $w_g^2 > F(\beta_i, \beta_e) > 0$ be satisfied in order to be unstable¹⁹. When $\beta > 2$, the system is unstable even if $w_g^2 < 0$.

We remark that when the fluid is *compressible* (i.e., $\nabla \cdot \mathbf{V} \neq 0$, which one usually associates with finite β), the ideal MHD energy principle states that the system can be unstable even when $w_g^2 < 0$, i.e., compressibility is *destabilizing* [25]. This seems to be inconsistent with the above result unless $\beta > 2$. Perhaps this is a consequence of using the local approximation and ballooning ordering, or perhaps one should distinguish between finite- β and compressibility. Low- β systems, like tokamaks, may exhibit finite- β effects even though the fluid is essentially incompressible (because of the large magnetic field). Perhaps significant effects of compressibility, such as the destabilization of the g -mode, only manifest themselves when $\beta \sim O(1)$. This would make the result of the previous paragraph at least *not inconsistent* with the energy principle. Or, maybe it's just a mistake.

Moving right along, we now consider same finite- β ideal MHD system, but with $\alpha_z > 0$. The low order dispersion relation is again a quadratic in w^2 of the form $w^4 - bw^2 + c = 0$, and c is the product of the roots $w_+^2 w_-^2$. The condition for instability is $c < 0$. The coefficient c is a complicated function of α_z , β_i , β_e , and w_g^2 , and again we revert to graphical analysis for a given set of parameters. The behavior of the solutions w_\pm^2 as functions of α_z is shown in Figure 16 for the specific parameters $\beta_e = 0.04$, $\beta_i = 0.01$, and $w_g^2 = 0.03$. The coefficient $c = w_+^2 w_-^2$ (Figure 16a) is negative for $\alpha_z < 0.1$, indicating instability. It is positive for $\alpha_z > 0.1$, so that either both roots are stable, or both roots are unstable. The individual roots w_+^2 and w_-^2 are shown in Figure 16b; $w_+^2 > 0$ for all α_z , and $w_-^2 > 0$ for $\alpha_z > 0.1$. Therefore, for these parameters, the finite- β ideal MHD g -mode is stabilized for $\alpha_z > 0.1$. Since the zero- β ideal MHD case is *not* stabilized by shear Alfvén waves, stability at $\beta > 0$ may be due to the generation of parallel sound waves.

We now consider two-fluid and FLR effects, $\delta_i > 0$. When $\alpha_z = 0$, the low order dispersion relation is a quintic that factors as

$$\left[w - \alpha_y \delta_i \left(w_g^2 + \frac{1}{2}\beta \right) \right] \left[w - \frac{1}{2} \alpha_y \delta_i \beta_i \left(1 + w_g^2 + \frac{1}{2}\beta \right) \right] f_3(w) = 0, \quad (84)$$

¹⁹Again, recall that $w_g^2 > 0$ means that \mathbf{g} and ∇n_0 point in *opposite* directions.

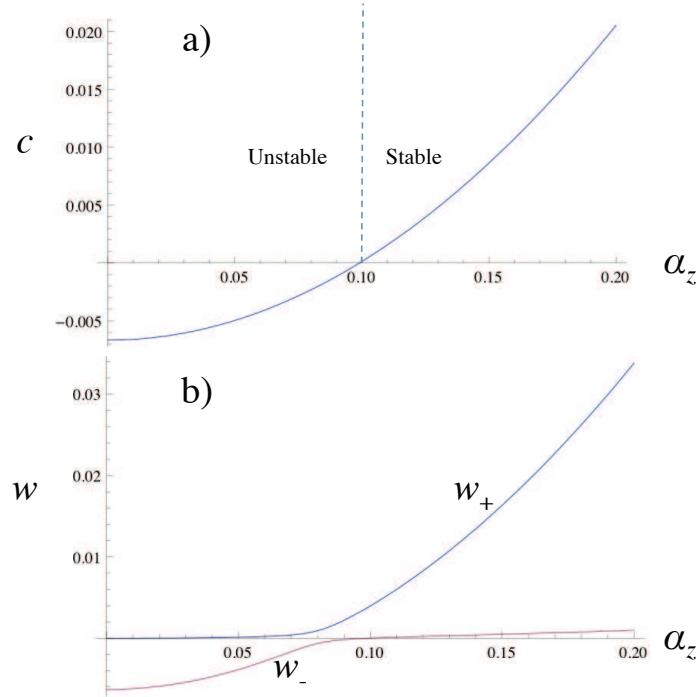


Figure 16: Illustrating the stabilization of the g -mode with parallel wave number α_z in finite- β ideal MHD, for the case $\beta_e = 0.04$, $\beta_i = 0.01$, and $w_g^2 = 0.03$. a) The coefficient $c = w_+^2 w_-^2$ of the zeroth degree term in the dispersion relation. For $\alpha_z < 0.1$, $c < 0$, the roots w_+^2 and w_-^2 have opposite signs, the negative root indicating instability. For $\alpha_z > 0.1$, $c > 0$ and the roots have the same sign; they are either both stable or both unstable. b) The roots w_+^2 and w_-^2 , showing that $w_+^2 > 0$ for all α_z , and $w_-^2 > 0$ for $\alpha_z > 0.1$. For these parameters, the finite- β g -mode is stabilized for $\alpha_z > 0.1$.

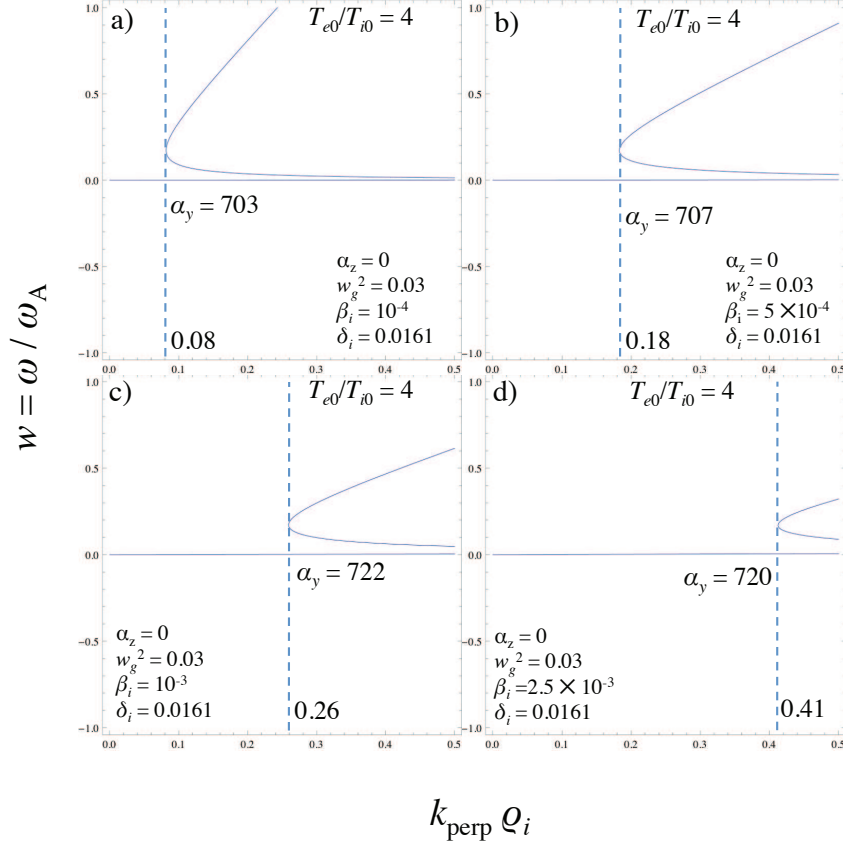


Figure 17: The locus of the roots of the two-dimensional, finite- β , two-fluid and FLR g -mode dispersion relation, $f_3(w) = 0$, in the $(k_{\perp}\rho_i, w)$ plane; $k_{\perp}\rho_i$ has been varied by changing α_y with fixed β and δ_i . Plots for four different values of β_i are shown. All have $T_{e0}/T_{i0} = 4$ and $\alpha_z = 0$ (two-dimensional). The stabilizing value if $k_{\perp}\rho_i$ is indicated by a dashed line, and a numerical value. In the middle of each figure is the corresponding value of α_y . This is almost the same for all cases. In all cases the horizontal axis is $0 \leq k_{\perp}\rho_i < 0.5$. a) $\beta_i = 10^{-4}$, $(k_{\perp}\rho_i)_{crit} = 0.08$, $(\alpha_y)_{crit} = 703$; b) $\beta_i = 5 \times 10^{-4}$, $(k_{\perp}\rho_i)_{crit} = 0.18$, $(\alpha_y)_{crit} = 707$; c) $\beta_i = 10^{-3}$, $(k_{\perp}\rho_i)_{crit} = 0.26$, $(\alpha_y)_{crit} = 722$; d) $\beta_i = 2.5 \times 10^{-3}$, $(k_{\perp}\rho_i)_{crit} = 0.41$, $(\alpha_y)_{crit} = 720$.

where $\beta = \beta_e + \beta_i$, and $f_3(w)$ is a full cubic. The first two factors are drift waves; the first factor is analogous to the first factor in Equation (78).

When $\delta_i > 0$, both two-fluid terms (Hall and electron pressure) and FLR terms (ion gyro-viscous stress and ion diamagnetic heat flux) enter the analysis. However, when $\alpha_y \rightarrow 0$, the solution is identical to Equation (82), i.e., it is independent of δ_i ; the important parameter seems to be $\alpha_y \delta_i$. Again, this is not surprising since drift vanishes when this product is zero.

The influence of two fluid effects at zero- β depends only the single parameter $\delta_i \equiv d_i/L_{n0} \sim 1\sqrt{n_0}$. In contrast, the FLR terms depend of $k_\perp \rho_i$, and the specific forms of the terms are only valid when $k_\perp \rho_i = \alpha_y \delta_i \sqrt{\beta_i/2} \sim \sqrt{T_{i0}/B_0} \ll 1$. Now three parameters, α_y , δ_i , and β_i , can affect the stability. Since the validity of the model depends on the smallness of the single parameter $k_\perp \rho_i$, we analyze the roots of $f_3(x) = 0$ as a function of $k_\perp \rho_i$ by varying α_y and keeping δ_i and β_i fixed.

In Figure 17 we plot the locus of the roots of $f_3(w) = 0$ in the $(k_\perp \rho_i, w)$ plane for the two-dimensional $\alpha_z = 0$, finite- β , two-fluid and FLR g -mode ($\delta_i = 0.0161$) with $T_{e0}/T_{i0} = 4$ and $w_g^2 = 0.03$, for four different fixed values of β . The dashed line and the number indicate the value of $(k_\perp \rho_i)_{crit}$ for stabilization. The corresponding value of $(\alpha_y)_{crit}$ is also given. The range of the horizontal axis is $0 < k_\perp \rho_i < 0.5$, which is marginally in the valid range $k_\perp \rho_i \ll 1$. In Figure 17a), $\beta_i = 10^{-4}$, and stabilization is achieved at $(k_\perp \rho_i)_{crit} = 0.08$; b) $\beta_i = 5 \times 10^{-4}$, and $(k_\perp \rho_i)_{crit} = 0.08$; c) $\beta_i = 10^{-3}$, and $(k_\perp \rho_i)_{crit} = 0.26$; and, d) $\beta_i = 2.5 \times 10^{-3}$, and $(k_\perp \rho_i)_{crit} = 0.41$.

We first note that the values of β are quite small; above these values $(k_\perp \rho_i)_{crit} > O(1)$ and the validity of the closures must be questioned. This is consistent with Figure 2 of Ref.[26], although somewhat different parameters were used. Second, the corresponding values of $\alpha_y = k_y L_{n0}$ are all ~ 700 , indicating stabilization at about the same value of α_y relatively independent of β when $\beta \ll 1$. This is consistent with Figure 1 of Ref.[26] for small β ; although, again, with different physical parameters. However, we cannot conclude that complete stabilization may be lost when $\beta > 0$, as reported in Ref.[26], since the value of β that is required for stabilization renders $k_\perp \rho_i$ too large for the model to be valid.

Finally, we consider the two-fluid, FLR, finite- β g -mode with $\alpha_z > 0$. As in Section 2.2, the low order dispersion relation is a full quintic. The locus of the roots in the (α_z, w) plane are shown in Figure 18. Stabilization is achieved for $\alpha_z > 0.118$. For these parameters, $k_\perp \rho_i = \alpha_y \delta_i \sqrt{\beta_i/2} = 0.143 \ll 1$

5.3 The Effect of Gravity on ITG-like Modes

We now turn to the effect of gravity on the η_i mode (or ITG-like mode) with $n_0(x) = e^x$ and $w_g^2 > 0$. Since the η_i mode requires finite- β , two-fluid and FLR effects, and $\alpha_z > 0$ to be unstable, we will not consider simpler cases, as in Section

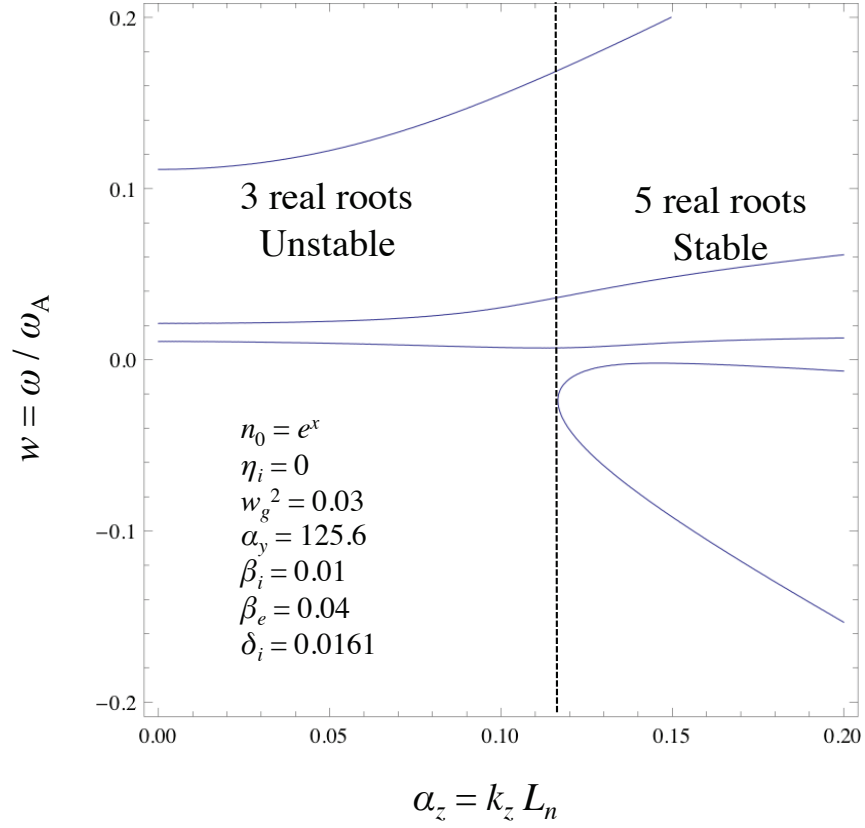


Figure 18: The locus of the roots of the three-dimensional, finite- β , two-fluid and FLR g -mode dispersion relation with $\alpha_z > 0$, in the (α_z, w) plane. For these parameters, the mode is stabilized for $\alpha_z > 0.118$.

5.2.

In Figure 19 we show the locus of the roots of the dispersion relation for the η_i mode with density gradient $n_0 = e^x$, but $w_g^2 = 0$. The presence of the two independent length scales L_{n0} and L_{Ti0} allows the system to distinguish between directions in x . As a consequence, the stability properties of the mode are now asymmetric with respect to $\eta_i = L_{n0}/L_{Ti0}$. The system remains stable for $\eta_i < 1.19 < 1.02$.

When $w_g^2 > 0$ and $\eta_i \neq 0$ simultaneously, we may expect the instability of the g -mode to destabilize the η_i mode at the same parameters. This is shown in Figure 20, where we plot the behavior of the roots for four different values of w^2 . As w_g^2 increases from 0.02 to 0.035, the stable region first shrinks (Figures 20a) and b), then shifts toward positive η_i (Figure 20c), and then disappears completely

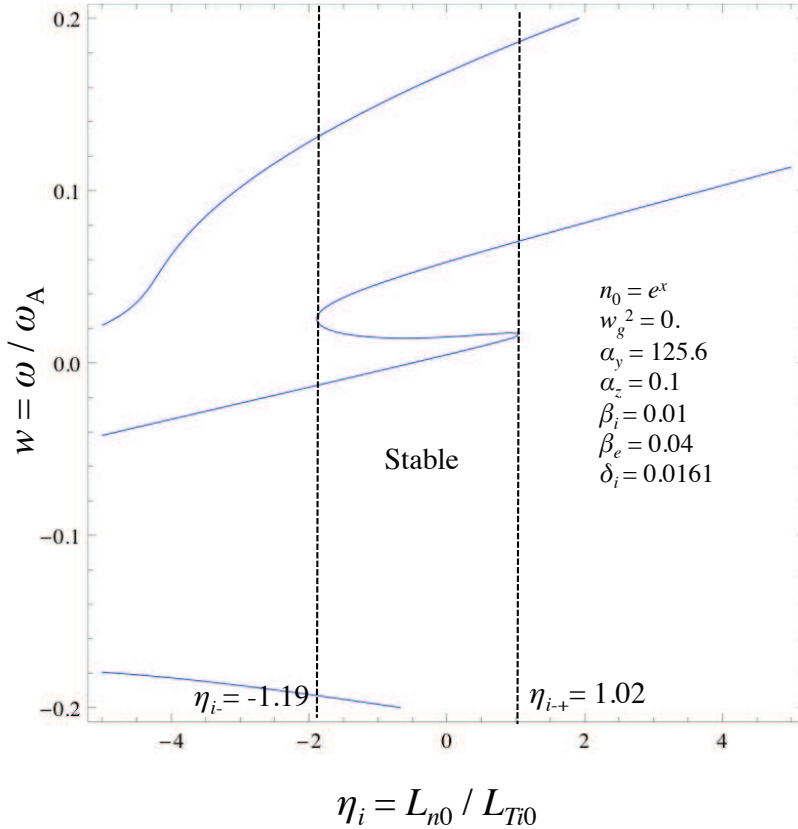


Figure 19: The locus of the roots of the η_i mode with $n_0 = e^x$ and $w_g^2 = 0$. The presence of the density gradient identifies a second direction in x and causes the instability to be asymmetric with respect to η_i . In this case, the configuration is unstable for $-1.19 < \eta_i < 1.02$.

(Figure 20d). We have not investigated in any detail the transition from Figure 20c) to Figure 20d).

6 Computational Results

The computational algorithm for solving the extended MHD equations has been described in detail elsewhere[17] and is implemented in the NIMROD code. The algorithm used here solves separate energy equations for the ions and adiabatic electrons. The full (Braginskii) gyro-viscous stress tensor and the ion diamagnetic

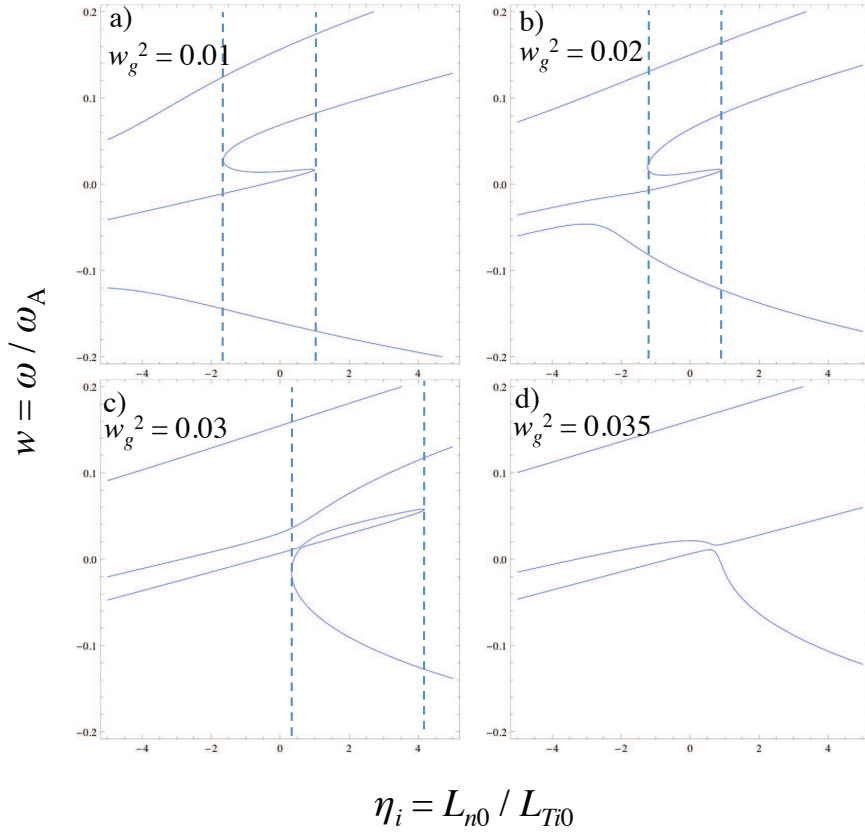


Figure 20: The locus of the roots of the η_i mode with $n_0 = e^x$ and $w_g^2 > 0$. The g -mode is unstable for $\eta_i = 0$, and the η_i mode needs $\eta_i > 0$ (along with finite- β and α_z). Here we show the locus of the roots in the (η_i, w) plane for the combined η_i - g -mode system at finite- β and $\alpha_z = 0.1$. a) At $w_g^2 = 0.01$ the η_i - g -mode remains stable for $-1.6 \leq \eta_i \leq 1.1$: b) At $w_g^2 = 0.02$, the stable region is $-1.1 < \eta_i < 0.9$, c) At $w_g^2 = 0.03$ the unstable region lies to the right of $\eta_i > 0$: $0.4 < \eta_i < 4.1$;, b) at $w_g^2 = 0.035$ the combined η_i - g -mode system is completely unstable (only three real roots).

heat flux are included. We seek verification of the algorithm by direct comparison of the computational solutions with the analytic solutions presented in Section 2. Of course, NIMROD solves the full differential system with no ordering, including solid boundaries in the x -direction, so *exact* agreement with the ordered local solution should not be expected. Approximate agreement is all that can be expected, and the extent of agreement will determine whether or not the model is verified.

6.1 Geometry and Equilibrium

The linearized extended MHD equations are solved as an initial value problem in slab geometry. For the computations, the equilibrium quantities vary in the x -direction, and we choose to orient the total wave vector \mathbf{k} in the z -direction, so that $\mathbf{k} = k_z \hat{\mathbf{e}}_z$. The equilibrium magnetic field is $\mathbf{B}_0(x) = B_{0y}(x) \hat{\mathbf{e}}_y + B_{0z}(x) \hat{\mathbf{e}}_z$. It is oriented in the (y, z) plane, and rotated from the direction of \mathbf{k} by an angle θ_b . The wave vector \mathbf{k} then has projections k_{\parallel} and k_{\perp} with respect to \mathbf{B}_0 that are determined by the rotation angle θ_b . The ion drift velocity is in the opposite direction from \mathbf{k}_{\perp} . The geometry is sketched in Figure 21. In this configuration, $k_y = 0$ always, and the perturbations vary as $f(x, z, t) = \hat{f}(x, t) e^{ik_z z}$, so that the problem becomes two-dimensional in the (x, z) plane. The wavefronts of the perturbation are parallel to the y -axis, depend only on x , and propagate in the direction of \mathbf{k} , i.e. z . The z -dimension is periodic, and perfectly conducting impermeable walls are places at $\pm x_{max}$ (not shown in the figure).

In the computations the equilibrium ion temperature varies as

$$T_{i0}(x) = T_{i0}(0) \left[1 + 0.9 \tanh \frac{x}{L_{Ti0}} \right]. \quad (85)$$

This model has little variation near the top and bottom boundaries in x , thus allowing the boundaries to be placed far from the location of the maximum gradient ($x = 0$) without the temperature becoming exponentially large or small, while minimizing both physical and numerical boundary effects. The equilibrium pressure profile for three different values of $1/L_{Ti0}$ are shown in Figure 22. The physical parameters are $n_0 = 10^{20}/\text{m}^3$, $B_0 = 2$ T, $T_{e0} = 1.9$ KeV, $T_{i0}(0) = 0.5$ KeV, $\beta_i = 0.01$, $\beta_e = 0.04$, $V_A \equiv B_0/\sqrt{\mu_0 M n_0} = 3.08 \times 10^6$ m/sec, where M is the proton mass (a hydrogen plasma), and $d_i \equiv c/\omega_{pi} = 0.0161$ m. The magnetic field and current density profiles are determined from force balance.

The analytic solution in the local approximation depends only on the *local* values of the parameters of the problem, and we have verified that the equilibrium of Equation (85) yields the same low order local dispersion relation as the exponential profile used in Section 2. For comparison with the local analytical results, we have used the solutions of Equation (46). As discussed in the footnote in the paragraph following Equation (8), when converting the dimensionless variables of

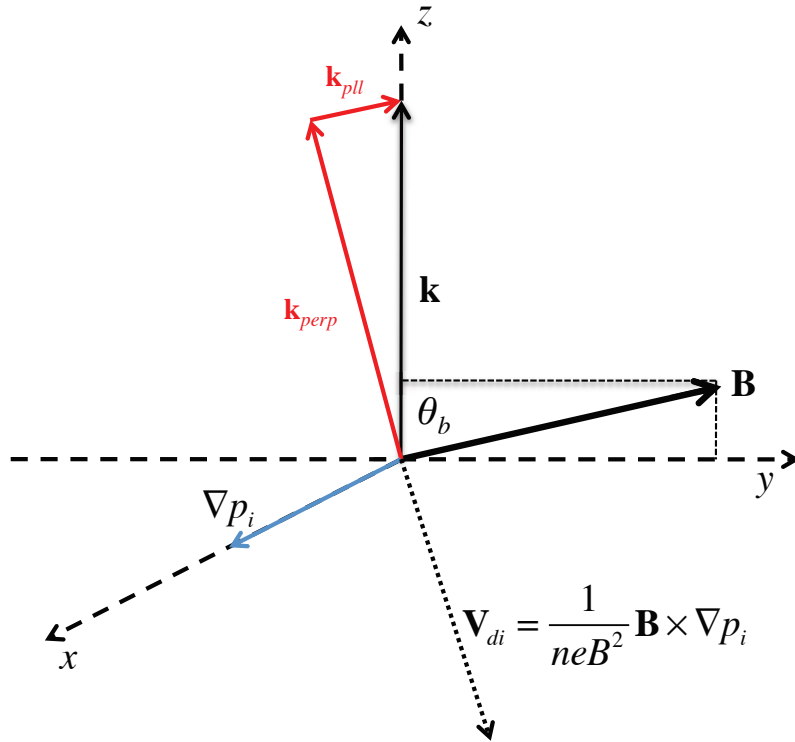


Figure 21: Geometry for the computational problem. By orienting the wave vector \mathbf{k} in the z -direction, and tilting \mathbf{B}_0 slightly out of the (x, y) plane, the problem becomes independent of the y -coordinate. The orientation of k_{\perp} , k_{\parallel} , the ion pressure gradient, and the ion drift velocity are shown. The vectors \mathbf{k} , \mathbf{k}_{\perp} , \mathbf{B} , and \mathbf{V}_{di} lie in the (y, z) plane.

the analytic solution to SI units for comparison with computational results, we must normalize distance to $a = L_{Ti0}$ so that $\eta_i = 1$, $\alpha_y = k_y L_{Ti0}$, $\alpha_z = k_z L_{Ti0}$, and $\delta_i = d_i / L_{Ti0}$. Further, the equilibrium of Equation (85) has an effective inverse scale length of $L_{Ti0eff}^{-1} = 0.9L_{Ti0}^{-1}$, which must be taken into account.

6.2 Computational Model

The equilibrium is subjected to a small perturbation $f(x, z) = f(x)e^{ik_z z}$. The perturbations have no y -dependence. In the NIMROD code, the time dependent

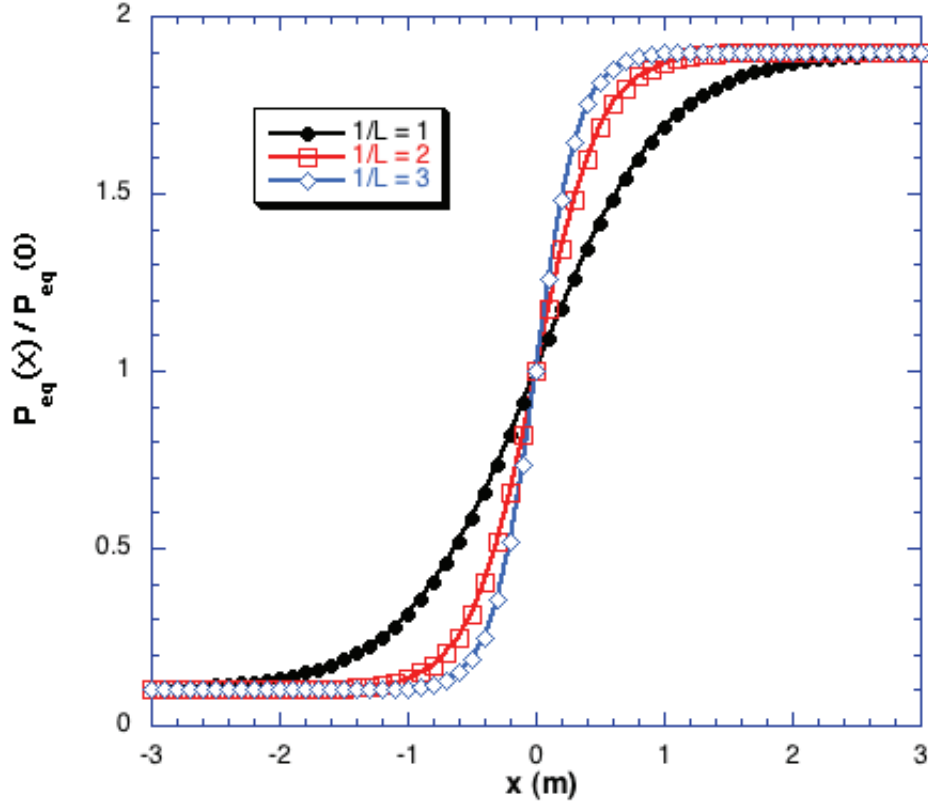


Figure 22: Equilibrium profile for three different values of $1/L_{Ti0}$ corresponding to the temperature profile of Equation (85).

equations are solved on an (x, y) grid of finite elements with arbitrary polynomial degree (here we choose 3), with periodic boundary conditions in y ; the z -direction is assumed periodic and approximated by finite Fourier transforms. Since there is no dependence on y , we use a minimal number of finite element nodes (3) in that dimension. The total wave number k_z and the angle θ_b are specified parameters, and the parallel and perpendicular components are $k_\perp = k_z \sin \theta_b$ and $k_\parallel = k_z \cos \theta_b$. In practice we specify the desired k_\parallel and k_\perp and then compute $k_z = \sqrt{k_\parallel^2 + k_\perp^2}$ and $\theta_b = \tan^{-1}(k_\perp/k_\parallel)$. The linearized extended MHD equations are then integrated forward in time. The fastest exponentially growing solution (if there is one) will emerge from the initial perturbations as $t \rightarrow \infty$.

The computational algorithm solves the differential equations of the extended MHD model including full x -dependence of the perturbations, and imposes boundary conditions at $x = \pm x_{wall}$. Neither of these are included in the analysis of Section 2; in the computations the local approximation is not assumed, and the computational solutions may have rapid x -variation. Since the fundamental algorithm has very low inherent numerical dissipation[8, 17], we have found it necessary to introduce a small amount of dissipation in the form of electrical resistivity, viscosity, and isotropic thermal conductivity. The particular values correspond to a Lundquist number $S = 10^9$, magnetic Prandtl number $P_{rM} = 1$. We have also found it useful to increase the resistivity and viscosity by a factor of 10^2 in a small layer near $\pm x_{wall}$. A small amount of hyper-diffusivity is used in the continuity equation: $D_{nh} = 10^{-2} \text{ m}^4/\text{sec}$. The boundary conditions at $\pm x_{wall}$ are: no-slip ($\mathbf{V} = 0$), $B_n = 0$, $E_{tan} = 0$, and Dirichlet conditions (fixed values) for density and temperature. We make a series of runs and keep all parameters fixed except L_{Ti} . The results are converged in time and spatial resolution, and dissipation. If there is an unstable mode, we determine its growth rate γ as a function of $1/L_{Ti}$.

Because of the x -variation in Equation (85), the values of the parameters affecting the analytic solution also vary with x ; some parts of the profile may be more unstable than others, and most of the profile is locally stable. The variation of L_{Tief}^{-1} with x for the case $L_{Ti0}^{-1} = 1 \text{ m}^{-1}$ is shown in Figure 23. Note that $L_{Ti0}^{-1}(0) = 0.9 \text{ m}^{-1}$, as discussed in Section 6.1. In Figure 24 we plot the variation of the ratio T_{e0}/T_{i0} with x for the same case. Each of these parameters can affect the local stability.

6.3 Stability as a Function of Equilibrium Scale Length

6.3.1 Growth Rates

For the given parameters, the analytic local growth rate depends on the local value of x . This is illustrated in Figure 25, where we plot the analytical, local growth rate of the unstable mode as each x for three different values of $1/L_{Tief}$. The

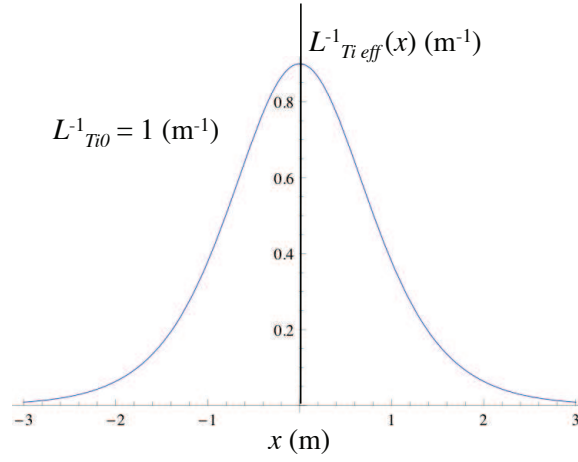


Figure 23: Variation of the inverse scale length with x for the equilibrium given by Equation (85) with $L^{-1}_{Ti0} = 1$ m^{-1} .

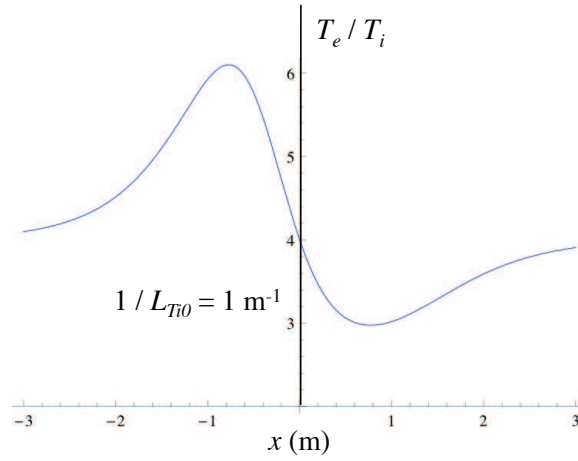


Figure 24: Variation of the the ratio of the electron and ion temperatures with x for the equilibrium given by Equation (85) with $L^{-1}_{Ti0} = 1$ m^{-1} .

growth rate envelope clearly increases with increasing $1/L_{Tieff}$, and appears to shift toward negative x as this parameter is increased, although the overall bias is toward $x > 0$. Note that the majority of the profile remains stable.

The NIMROD code also obtains an unstable mode whose growth rate is a function of $1/L_{Tieff}$. Of course, the computational result is a *global* mode, so direct comparison with the local analytical results is problematical. This comparison is illustrated in Figure 26, where we plot the NIMROD global growth rate, the analytical local growth rate at $x = 0$, and the *average* of the local growth rate as a function of x (see Figure 25), as functions of the effective inverse scale length $1/L_{Tieff}$. All show a threshold in $1/L_{Tieff}$, although the NIMROD threshold is smaller than the others. (The average curve has a slightly smaller threshold than the local $x = 0$ curve because the profile first becomes unstable at $x = 0.2$.) The NIMROD growth rate starts larger than the local $x = 0$ value, but eventually becomes intermediate between the $x = 0$ value and the average of the local values. While the general behavior is similar, the quantitative connection between the

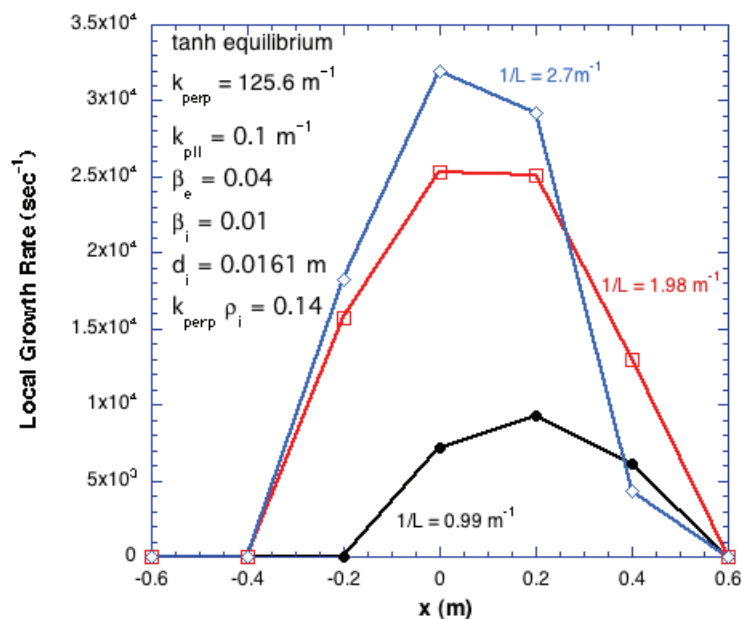


Figure 25: Analytic local growth rate as a function of x for three different values of $1/L_{Tieff}$. Most of the profile remains stable.

local growth rate and the global growth rate remains elusive. Given the local approximation, perhaps this is the best one can expect.

6.3.2 Global Eigenmode Structure

As discussed in Section 6.1, and sketched in Figure 21, the computational problem is two dimensional in the (x, z) plane, and is characterized as $f(x, t)e^{ik_z z}$. The eigenfunction $f(x, t)$ is determined by the solution of differential equations. The local analytic approximation is an algebraic formulation that gives no information about the spatial structure of the eigenfunction, so direct comparison is impossible.

The eigenfunctions of the perturbed ion temperature are shown as functions of x as determined by the NIMROD code for $1/L_{Ti0} = 1$, $1/L_{Ti0} = 2$, and $1/L_{Ti0} = 3$ in Figures 27, 28, and 29 respectively.

Three features of the eigenfunctions are apparent. First, they become more oscillatory as $1/L_{Ti0}$ increases. (The inset in Figure 29 shows the detailed structure

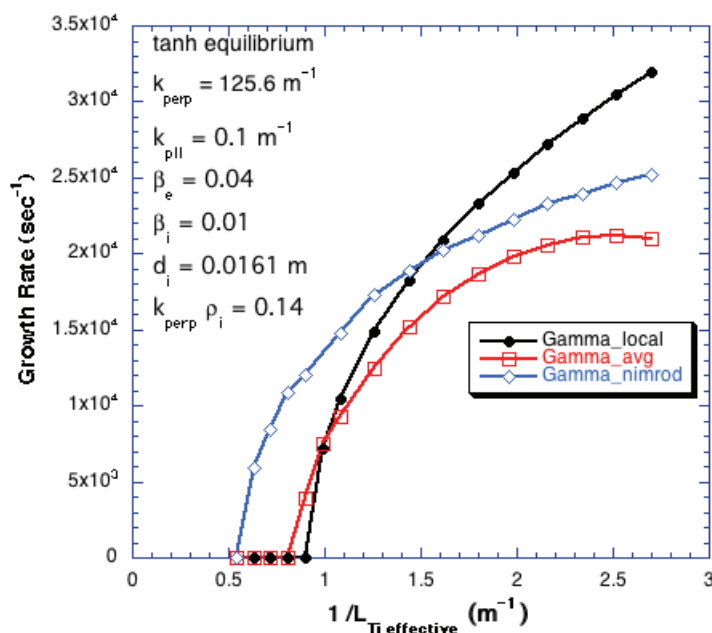


Figure 26: Analytic local growth rate at $x = 0$ (black), the local growth rate averaged over x (red) and the growth rate of the global mode as determined by NIMROD (blue), as functions of $1/L_{Tieff}$.

near $x = 0$.) This can be attributable to the increased shearing of the drift velocity ($V_{di} \sim dT_{i0}/dx \sim \text{sech}^2(x/L_{T_{i0}})/L_{T_{i0}}$) near $x = 0$. If the stable structures for small $1/L_{T_{i0}}$ were temperature perturbations symmetric about $x = 0$, they would be symmetrically sheared in the direction of \mathbf{k}_\perp by the x dependent drift velocity, the amount of distortion increasing with increasing $V_{di}(x)$. This shearing manifests itself as oscillations in x whose spatial frequency increases with $1/L_{T_{i0}}$.

Second, none of the eigenfunctions are centered at $x = 0$, in spite of the fact that the maximum of the drift velocity occurs there ($V_{di} \sim 1/L_{tieff}$; see Figure 23). Instead, they are biased toward negative x , even though the *local* growth rate is biased toward positive x ; see Figure 25. The local growth rate depends on a combination the destabilizing influences of $1/L_{T_{i0}}$ and the temperature ratio T_{e0}/T_{i0} ; the local growth rate increases with the former and decreases with the latter above $T_{e0}/T_{i0} \sim 1$; see Figure 30. The inverse scale length is symmetric in x , but the asymmetry of temperature ratio (see Figure 24) should make $x > 0$ *more* unstable; this is consistent with the x -dependence of the local growth rate. Nonetheless, the global eigenfunction as determined by the NIMROD code is biased toward $x < 0$. There seems to be little correlation between the variation of the local growth rate with x and the shape of the global eigenfunction.

Finally, it seems clear that the local approximation becomes worse as $1/L_{T_{i0}}$ is increased, if it is valid at all. Perhaps this accounts for quantitative differences in the results.

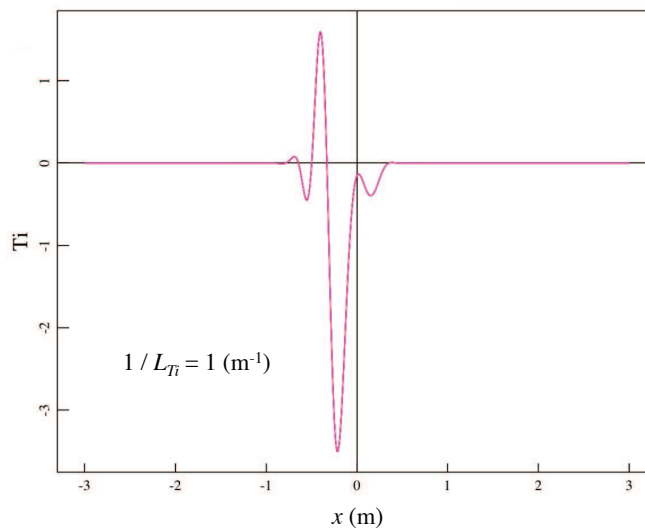


Figure 27: Eigenfunction of the perturbed ion temperature as a function of x for the case $1/L_{T_{i0}} = 1$.

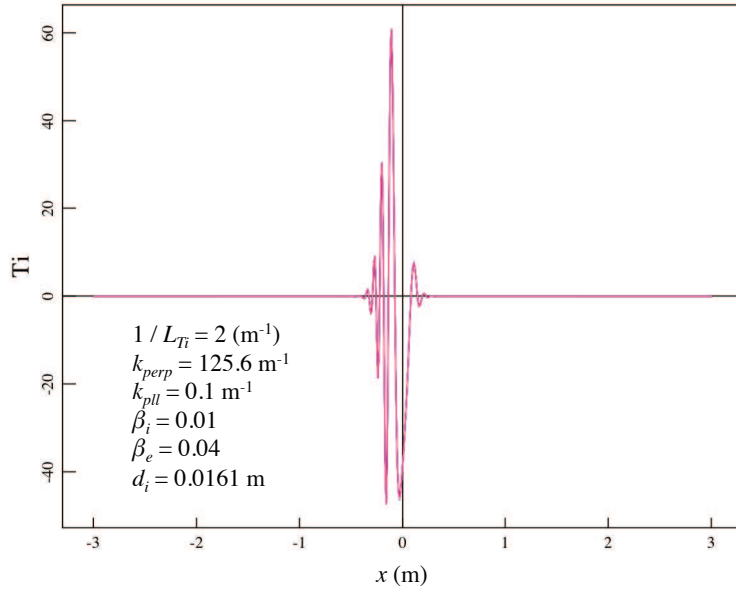


Figure 28: Eigenfunction of the perturbed ion temperature as a function of x for the case $1/L_{Ti0} = 2$.

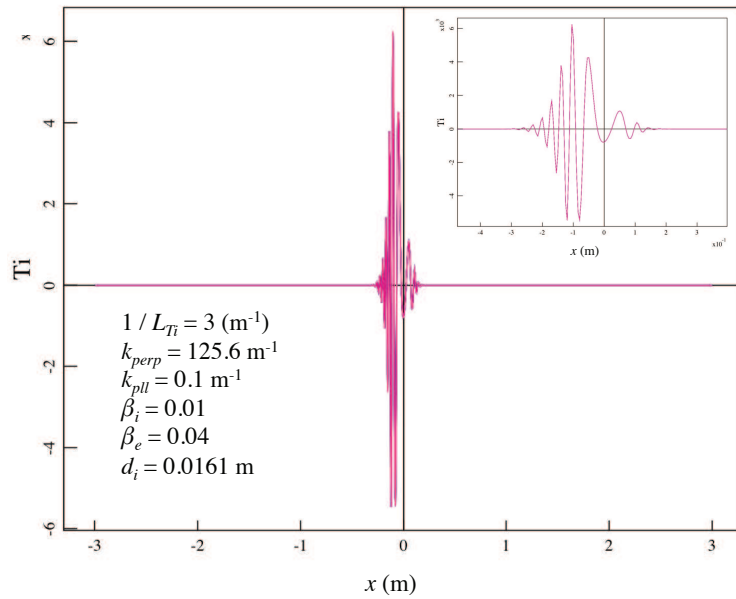


Figure 29: Eigenfunction of the perturbed ion temperature as a function of x for the case $1/L_{Ti0} = 3$. The inset shows the detailed structure near $x = 0$.

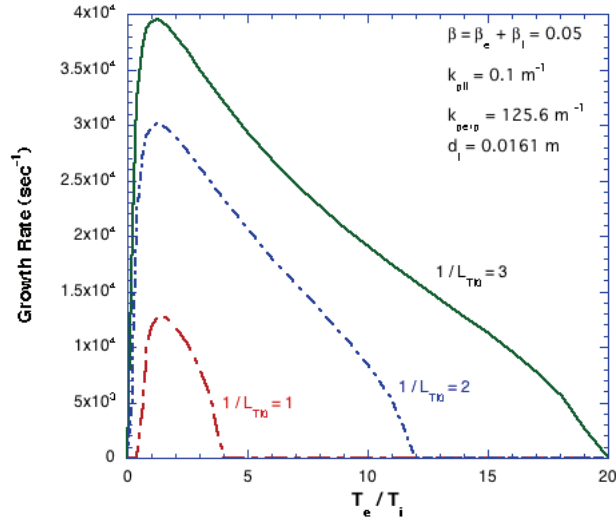


Figure 30: Analytic local growth rate as determined by Equation (46) as a function of T_{e0}/T_{i0} for three different values of $1/L_{T_{i0}}$. The local growth rate slowly *decreases* with increasing temperature ratio above $T_{e0}/T_{i0} \sim 1$.

6.4 Stability as a Function of $k_{\perp}\rho_i$

We have also examined the stability as a function of $k_{\perp}\rho_i$; the validity of the model requires $k_{\perp}\rho_i \ll 1$. (Since $k_{\perp}\rho_i = \alpha_{\perp}\delta_i\sqrt{\beta_i/2}$, the value of $k_{\perp}\rho_i$ can varied by changing the normalized perpendicular wave number $\alpha_{\perp} = k_z L_{Ti0} \cos \theta_b$ while keeping the remaining parameters constant.) In this case comparison with the local analytical growth rate is possible. This is shown in Figure 31, where both the local analytical and global computational growth rates are shown as functions of $k_{\perp}\rho_i$ for the range $0 < k_{\perp}\rho_i < 0.5$.

Both solutions indicate a threshold in $k_{\perp}\rho_i$ for instability, although the computational value ($k_{\perp}\rho_i \sim 0.05$) is smaller than the analytical value ($k_{\perp}\rho_i \sim 0.1$). This is a reflection of the stability of the system in ideal and Hall MHD (i.e. $k_{\perp}\rho_i \rightarrow 0$). This ITG-like mode requires both two-fluid (extended Ohm's law) and FLR effects (gyro-viscosity and diamagnetic heat flux) for instability; see the discussion in Section 2.1. This property is reproduced qualitatively in the computations. The computational and analytical growth rates have roughly comparable values for $k_{\perp}\rho_i < 0.3$, and diverge above this value. However, for these parameters the fluid model becomes increasingly unreliable as $k_{\perp}\rho_i$ is increased, and the comparison between the computational and analytical growth rates likely becomes

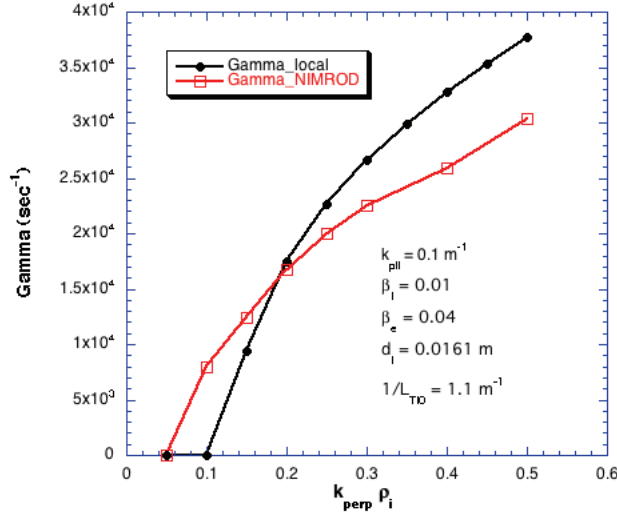


Figure 31: Local analytical (black) and global computational (red) growth rates as functions of $k_{\perp}\rho_i$.

moot.

There is reasonable agreement between the growth rates for values of $k_{\perp}\rho_i$ where the fluid model is valid. Quantitative difference may be attributed to the spatial variation of the equilibrium in the computational model, and the validity of the local approximation in the analytical model.

The monotonic increase in the growth rate with $k_{\perp}\rho_i$ has implications for future non-linear computations. A major difficulty in these problems is attaining sufficient spatial resolution to resolve the spectrum of fluctuations. When these arise from turbulent motions, they cascade to larger k by nonlinear coupling, where they are eventually dissipated at wave number k_{dis} . The spatial resolution of the computation must be sufficient to resolve this dissipation scale. Even with modern super-computers, this is often difficult (or impossible) with realistic values of dissipation. The problem becomes more difficult when the spectrum of fluctuations is due to linear instabilities whose growth rate increases with increasing k . This is the case for interchange-type modes (e.g., g -modes or resistive interchange/ballooning modes; see Section 5.2). However, those modes are unstable in ideal (or resistive) MHD, and two-fluid and FLR effects are *stabilizing* at large k , providing a natural cut-off for the spectrum. In the present case of ITG-like modes, the instability of the system is *caused* by two-fluid and FLR effects, so there is no natural cut-off. Increasing the dissipation (such as collisional viscosity, $\sim \nu k^2$) to resolve the short wavelengths affects the long wavelengths as well, and this approach is generally considered unsatisfactory. In this case it is necessary to introduce a *hyper-dissipation* term ($\sim k^4$) that dissipates (or stabilizes) the high- k modes while minimally affecting the dynamics at low- k . Development of such a term is likely necessary if fluid models are to attempt to simulate ITG-like turbulence.

6.5 Stability as a Function of Electron β Fraction

As discussed in Section 2.1.6, and shown in Figure 1, the stability of the system depends on the electron β fraction $f_e = \beta_e/(\beta_e + \beta_i)$, with (near) stability for both $f_e = 0$ and $f_e = 1$. Results are shown in Figure 32, where we plot the analytical growth rate (solution of Equation (40))(red curve) and the growth rate determined by the NIMROD code (black dots), as a function of the electron β fraction for $\beta = \beta_e + \beta_i = 0.05$. NIMROD indicates stability when the electrons are cold, in qualitative agreement with kinetic theory [2, 6].

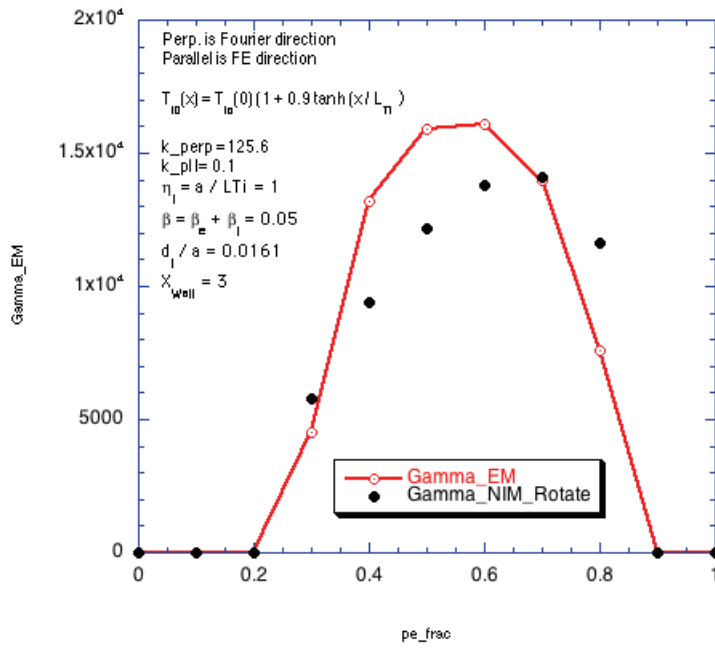


Figure 32: Growth rate as a function of the electron temperature fraction, $f_e = \beta_e / (\beta_i + \beta_e)$, for fixed $\beta = \beta_i + \beta_e = 0.05$ and $\eta_i = 1.2$. The other parameters are $\alpha_y = 126.5$, $\alpha_z = 0.1$, and $\delta_i = 0.0161$. The red curve is Equation (40). The black dots are the results of NIMROD simulations with both gyro-viscosity and diamagnetic heat flux.

7 Discussion

The dynamics of a magnetized plasma are described by the evolution of the distribution functions according to the plasma kinetic equation (PKE) for each species. This kinetic model contains a large number of degrees of freedom. These can be reduced by considering the evolution of the velocity moments of the distribution functions and the corresponding PKEs. The two-fluid model considers the dynamics of only a few of these lowest order moments that introduce the lowest order corrections (in $k_{\perp}\rho_i$) to ideal MHD. Here we are concerned with how well computational solutions obtained with the extended MHD code NIMROD agree with approximate analytic solutions of the same equations, as well as how well these solutions of the two-fluid/FLR (extended MHD) model correspond to the solutions of the underlying PKEs.

We have analyzed the stability of the two-fluid model using the local approximation for the case in Cartesian slab geometry where there is no shear in the magnetic field and the equilibrium density and electron temperature are spatially uniform, but there is a gradient in the equilibrium ion temperature. There can be instability if the temperature gradient is sufficiently large. This configuration is stable in ideal MHD; it is destabilized by effects of finite ion Larmor radius (FLR). It is therefore a good test case for judging the efficacy of using the extended MHD model for describing the dynamics of highly magnetized, hot, nearly collisionless plasmas.

Analytic solutions in the local approximation of the two-fluid equations have been obtained using both electro-static and electro-magnetic models. These are in excellent agreement, indicating that the instability is primarily electro-static. We have also verified that these are in agreement with local solutions of the extended MHD equations, to which they are mathematically equivalent.

The extended MHD equations contain terms in the ion momentum and energy equations, the gyro-viscous stress and the ion diamagnetic heat flux, that together approximate the effects of finite ion Larmor radius on the global dynamics of the plasma. The terms enter the theory at the same order (in $k_{\perp}\rho_i$), and they should both be included for the model to be consistent. Together, their effect is to cancel at least some of the contributions to advection by the ion diamagnetic drift velocity; see Section 1.2. If they are both excluded (so-called Hall MHD) the system has stable solutions; see Section 2.1.5. If only the gyro-viscosity is retained the system is unstable, but the instability persists in the limit $\beta_e \rightarrow 0$; Section 2.1.4. When they are both retained, either exactly or approximately, the system is unstable, but is stable when $\beta_e \rightarrow 0$; Sections 2.1.2 and 2.1.3. This latter result is in qualitative agreement with the predictions of kinetic theory [2, 6].

The gyro-viscous stress tensor depends on the spatial variation of both the ion velocity and the ion diamagnetic heat flux[11, 20, 21, 22]. However, for the

parameters of this problem the heat flux contribution is one order higher in the small parameter ρ_i/L_{Ti0} , so it does not affect the results to lowest order, and it is consistent to ignore these terms in the computational model.

We have used the extended MHD code NIMROD to obtain global linear solutions for the same geometry and physical parameters, and have compared the resulting growth rates with those obtained from the local analytic theory. Reasonable agreement has been obtained for the growth rate as a function of the inverse equilibrium ion temperature scale length $1/L_{Ti0}$, the FLR parameter $k_\perp\rho_i$, and the electron β fraction, $f_e = \beta_e/(\beta_e + \beta_i)$.

Since there is no natural stabilizing mechanism at high- k , the calculated monotonic increase in the growth rate with $k_\perp\rho_i$ indicates that there may be difficulties in resolving the spectrum of turbulence in non-linear computations. The development of a satisfactory hyper-dissipation model is likely necessary for this type of problem.

The local analytic solution does not predict the shape of the eigenfunction $\tilde{f}(x)$; only the local growth rate can be calculated. However, the local growth rate can be obtained as a function of x , and one might expect some correlation between the most unstable regions of the profile and the shape of the global eigenfunction produced by the NIMROD computation. Here there is a discrepancy between the analytic and computational solutions. The analytic solution implies that the eigenfunction should be biased toward $x > 0$, while the computational eigenfunctions are biased toward $x < 0$. We have no explanation for this difference. The computational eigenfunctions exhibit oscillatory structure in x , which can be qualitatively explained as shearing of the perturbation by the x dependent ion drift velocity. In any case, the rapid spatial oscillations in the computational eigenfunctions indicate that the local approximation used in the analytic solution may not be valid. Perhaps this accounts for the differences.

We conclude that the NIMROD code has been verified for this problem to the extent that both the fluid models and the local analytic solutions are accurate.

There is the final question of how well the full two-fluid model agrees with kinetic theory over a range of parameters, i.e., β_i , β_e , $k_\perp\rho_i$, etc. This can best be determined by running the same problem with a kinetic code and comparing with the two-fluid (extended MHD) results in detail.

Progress in extending fluid models further into the kinetic regime requires the implementation of more accurate (i.e., higher order in $k_\perp\rho_i$) closure schemes for the ion stress tensor and heat flux. Presumably these would incorporate effects of ion Landau damping [14], which have not been considered here. The problem of ITG-like modes analyzed here is a good test case of these models.

References

- [1] L. I. Rudakov and R. Z. Segdeev, *Soviet Phys. - Doklady* **6**, 415 (1961).
- [2] B. Coppi, M. N. Rosenbluth and R. Z. Segdeev, *Phys. Fluids* **10**, 582 (1967).
- [3] C. C. Hegna, Lecture notes, undated, private communication (2011).
- [4] C. R. Sovinec, private communication (2011).
- [5] Jan Weiland, *Collective Modes in Inhomogeneous Plasma*, Institute of Physics Publishing, Bristol and Philadelphia, 2000.
- [6] T. H. Stix, *Waves in Plasmas*, Second Edition, Problems 3.5, 14.6 and 14.7, AIP, 1992.
- [7] F. Cajori, *An Introduction to the Theory of Equations*. Dover, New York, 1969.
- [8] C. R. Sovinec, A. H. Glasser, T. A. Gianakon, D. C. Barnes, R. A. Nebel, S. E. Kruger, D. D. Schnack, S. J. Plimpton, A. Tarditi, M. S. Chu and the NIMROD Team, *J. Comput. Phys.* **195**, 355 (2004).
- [9] S. C. Jardin, J. Breslau and N. Ferraro, *J. Comput. Phys.* **226**, 2146 (2007).
- [10] D. D. Schnack, D. C. Barnes, D. P. Brennan, C. C. Hegna, E. Held, C. C. Kim, S. E. Kruger, A. Y. Pankin and C. R. Sovinec, *Phys. Plasmas* **13**, 158103 (2006).
- [11] R. D. Hazeltine and J. D. Meiss, *Plasma Confinement*, pp. 208ff, Addison-Wessley, Redwood City, 1992.
- [12] P. N. Guzdar, L. Chen, W. M. Tang and P. H. Rutherford, *Phys. Fluids* **26**, 673 (1983)
- [13] S. C. Guo and J. Weiland, *Nucl. Fusion* **37**, 1095 (1997).
- [14] G. W. Hammet and F. W. Perkins, *Phys. Rev. Letters* **64**, 3019 (1990).
- [15] S. E. Parker, W. Dorland, R. A. Santoro, M. A. Beer, Q. P. Liu, W. W. Lee and G. W. Hammet, *Phys. Plasmas* **1**, 1461 (1994).
- [16] Mathematica, V6.0.2.1, Copyright 2006-2008, Wolfram Research, Inc.
- [17] C. R. Sovinec, J. R. King, and the NIMROD Team, *J. Comput. Phys.* **229**, 5803 (2010).

- [18] C. C. Hegna, “ITG Modes in extended MHD II”, November 23, 2011 (unpublished).
- [19] C. R. Sovinec, “Yet Another Note on Fluid ITG, 2/15/12” (unpublished).
- [20] A. N. Simakov and P. J. Catto, *Phys. Plasmas* **12**, 012105 (2005).
- [21] J. J. Ramos, *Phys. Plasmas* **12**, 052102 (2005).
- [22] J. J. Ramos, *Phys. Plasmas* **12**, 112301 (2005).
- [23] J. W. Strutt (Lord Rayleigh), *Proc. London Math. Soc.* **14**, 170 (1883).
- [24] K. V. Roberts and J. B. Taylor, *Phys. Rev. Letters* **8**, 197 (1962).
- [25] D. D. Schnack, *Lectures in Magnetohydrodynamics* pp. 171ff, Springer-Verlag, Heidelberg Berlin, 2009.
- [26] P. Zhu, D. D. Schnack, F. Ebrahimi, E. G. Zweibel, M. Suzuki, C. C. Hegna, and C. R. Sovinec, *Phys. Rev. Letters* **101**, 085005 (2008).